



# Computational Investigation of Structural Dynamics of SARS-CoV-2 Methyltransferase-Stimulatory Factor Heterodimer nsp16/nsp10 Bound to the Cofactor SAM

## OPEN ACCESS

### Edited by:

Arvind Ramanathan,  
Argonne National Laboratory (DOE),  
United States

### Reviewed by:

Shruthi Viswanath,  
National Centre for Biological  
Sciences, India  
Om Choudhary,  
University of Pittsburgh, United States  
Filippo Pullara,  
Splintellx Inc., Pittsburgh,  
United States

### \*Correspondence:

Parimal Kar  
parimal@iiti.ac.in

†These authors have contributed  
equally to this work

### Specialty section:

This article was submitted to  
Biological Modeling and Simulation,  
a section of the journal  
Frontiers in Molecular Biosciences

**Received:** 31 July 2020

**Accepted:** 23 October 2020

**Published:** 24 November 2020

### Citation:

Sk MF, Jonniya NA, Roy R, Poddar S  
and Kar P (2020) Computational  
Investigation of Structural Dynamics of  
SARS-CoV-2  
Methyltransferase-Stimulatory Factor  
Heterodimer nsp16/nsp10 Bound to  
the Cofactor SAM.  
Front. Mol. Biosci. 7:590165.  
doi: 10.3389/fmolb.2020.590165

**Md Fulbabu Sk<sup>†</sup>, Nisha Amarnath Jonniya<sup>†</sup>, Rajarshi Roy, Sayan Poddar and Parimal Kar\***

Discipline of Biosciences and Biomedical Engineering, Indian Institute of Technology Indore, Khandwa, India

Recently, a highly contagious novel coronavirus disease 2019 (COVID-19), caused by SARS-CoV-2, has emerged, posing a global threat to public health. Identifying a potential target and developing vaccines or antiviral drugs is an urgent demand in the absence of approved therapeutic agents. The 5'-capping mechanism of eukaryotic mRNA and some viruses such as coronaviruses (CoVs) are essential for maintaining the RNA stability and protein translation in the virus. SARS-CoV-2 encodes S-adenosyl-L-methionine (SAM) dependent methyltransferase (MTase) enzyme characterized by nsp16 (2'-O-MTase) for generating the capped structure. The present study highlights the binding mechanism of nsp16 and nsp10 to identify the role of nsp10 in MTase activity. Furthermore, we investigated the conformational dynamics and energetics behind the binding of SAM to nsp16 and nsp16/nsp10 heterodimer by employing molecular dynamics simulations in conjunction with the Molecular Mechanics Poisson-Boltzmann Surface Area (MM/PBSA) method. We observed from our simulations that the presence of nsp10 increases the favorable van der Waals and electrostatic interactions between SAM and nsp16. Thus, nsp10 acts as a stimulator for the strong binding of SAM to nsp16. The hydrophobic interactions were predominately identified for the nsp16-nsp10 interactions. Also, the stable hydrogen bonds between Ala83 (nsp16) and Tyr96 (nsp10), and between Gln87 (nsp16) and Leu45 (nsp10) play a vital role in the dimerization of nsp16 and nsp10. Besides, Computational Alanine Scanning (CAS) mutagenesis was performed, which revealed hotspot mutants, namely I40A, V104A, and R86A for the dimer association. Hence, the dimer interface of nsp16/nsp10 could also be a potential target in retarding the 2'-O-MTase activity in SARS-CoV-2. Overall, our study provides a comprehensive understanding of the dynamic and thermodynamic process of binding nsp16 and nsp10 that will contribute to the novel design of peptide inhibitors based on nsp16.

**Keywords:** SARS-CoV-2, nsp16/nsp10, molecular dynamics, PCA, MM-PBSA

## INTRODUCTION

Coronaviruses (CoVs) are considered as an etiological agent for causing severe acute respiratory syndrome (SARS) in humans. In the past two decades, SARS-CoV and MERS-CoV (middle east respiratory syndrome coronavirus) were responsible for the epidemic in 2003 and 2012, respectively. Recently, in December 2019, the novel coronavirus (COVID-19) pandemic, caused by SARS-CoV-2, first broke out in Wuhan city of China and has been spreading worldwide (Bogoch et al., 2020; Guan et al., 2020; Lin X. et al., 2020). So far, ~42 million people worldwide are infected by SARS-CoV-2, including ~1.1 million deaths. In India, the COVID-19 tally has already crossed 7.7 million, including ~0.1 million deaths. However, neither prophylactic vaccines nor any direct antiviral drugs are available to effectively treat the human and animal coronavirus disease (Lu, 2020; Pillaiyar et al., 2020; Sheahan et al., 2020).

CoVs are single-stranded positive-sense RNA viruses (Eckerle et al., 2010; Fehr and Perlman, 2015) belonging to the family *Coronaviridae* and possess the largest genome (26.4–31.7 kb) (Woo et al., 2010). They are classified into four genera, namely *Alphacoronaviruses*, *Betacoronaviruses*, *Gammacoronaviruses*, and *Deltacoronaviruses* (King et al., 2011). CoVs can infect both humans and animals (Lun and Qu, 2004; Coleman and Frieman, 2014), and can cause diseases like Hepatitis and Pneumonitis in mouse (Weiss and Leibowitz, 2011) and neurologic & respiratory diseases in humans (Arabi et al., 2015; Huang et al., 2020). So far, seven distinctive strains of human coronaviruses (HCoV) have been disclosed that includes 229E and NL63 (*Alphacoronaviruses*), and OC43, HKU1, SARS-CoV (2002), MERS-CoV (2012), and SARS-CoV-2 (2019) (*Betacoronaviruses*) (Weiss and Navas-Martin, 2005; Zeng et al., 2018; Singh et al., 2020). SARS-CoV-2 shares a strong correlation with the bat CoV RaTG13 having a 96.2% genome sequence identity, suggesting its possible evolution from bat CoVs (Wu et al., 2020; Zhou P. et al., 2020). SARS-CoV-2 displays a sequence similarity of 80% with SARS-CoV, whereas only 50% with MERS-CoV (Lu et al., 2020; Wu et al., 2020; Zhou Y. et al., 2020). Currently, most of the therapeutic options that are available for controlling COVID-19 is based on the previous knowledge and information gathered from SARS-CoV and MERS-CoV.

Most viruses or eukaryotic cellular mRNA possess the 5'-end capping mechanism that plays a vital role in mRNA splicing, translation initiation, stability, and intracellular RNA transport (Furuichi and Shatkin, 2000). The capping of the 5'-end occurs through a sequential enzymatic process. This involves three enzymes, such as RNA guanylyltransferase (GTase), RNA triphosphatase (TPase), and RNA guanine-N7-methyltransferase (N7-MTase). This generates a cap-0 structure (m7GpppN). It is further methylated at the 2'-O position of mRNA by 2'-O-methyltransferase (2'-O-MTase) and generates the cap-1 (m7GpppNm) and cap-2 (m7GpppNmNm) structures. This mimicking of the eukaryotic mRNA capping mechanism ultimately helps the virus evade the host innate immune system (Furuichi and Shatkin, 2000; Wang et al., 2015). Both the MTase uses S-adenosyl-L-methionine (SAM or AdoMet) as a donor

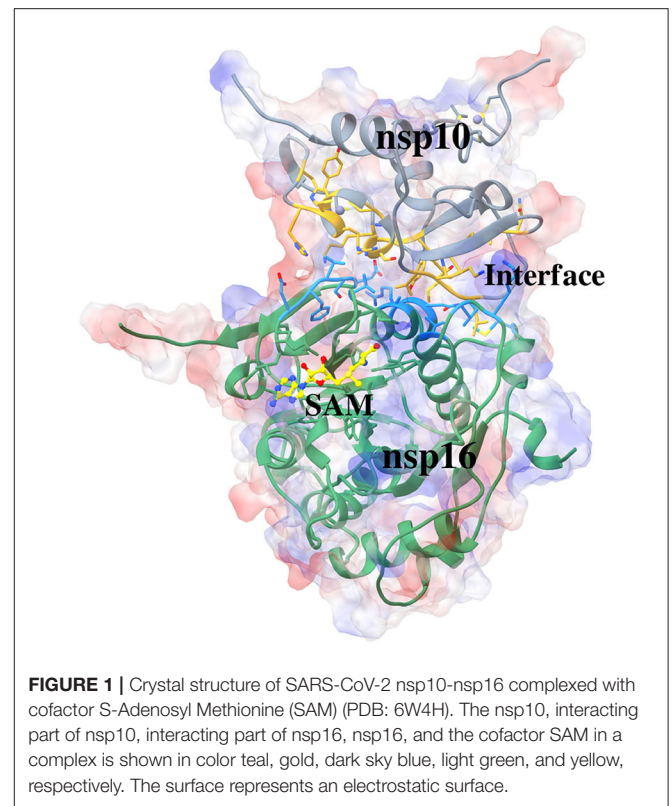


**FIGURE 1** | Crystal structure of SARS-CoV-2 nsp10-nsp16 complexed with cofactor S-Adenosyl Methionine (SAM) (PDB: 6W4H). The nsp10, interacting part of nsp10, interacting part of nsp16, nsp16, and the cofactor SAM in a complex is shown in color teal, gold, dark sky blue, light green, and yellow, respectively. The surface represents an electrostatic surface.

of methyl and gives a by-product, S-adenosyl-L-homocysteine (SAH or AdoHcy).

The genome of SARS-CoV-2 is comprised of 10 ORFs (Open Reading Frame). ORF1ab encodes the replicase polyprotein 1ab (PP1ab), which gets cleaved by the two viral proteases, PL<sup>PRO</sup> (papain-like protease) and 3CL<sup>PRO</sup> (3-C like protease) at the N-terminus and C-terminus, respectively, to form all the 16 non-structural proteins (nsp1, nsp2, nsp3 by PL<sup>PRO</sup>, and nsp4-nsp16 by 3CL<sup>PRO</sup>). The remaining ORFs are associated with encoding structural proteins, such as spike (S), envelope (E), membrane (M), and nucleocapsid (N) proteins, as well as other accessory proteins (Harcourt et al., 2004; Yang et al., 2005; Chen et al., 2020; Wu et al., 2020). Previous structural and biochemical characterization studies on SARS-CoV (2002) showed that in the nsp10-nsp16/SAM complex, nsp10 enhances the methylase activity of nsp16 by increasing the stability of the SAM-binding pocket (Chen et al., 2011; Wang et al., 2015).

The present study involves analyzing protein-protein interactions in the heterodimeric structure formed by nsp10 and nsp16 of SARS-CoV-2. The recently solved crystal structure of SARS-CoV-2 nsp16/nsp10 heterodimer bound to SAM (PDB: 6W4H) (Minasov et al., 2020) is used in the current study. The three-dimensional structure of the complex is shown in **Figure 1**. Here, we have used the standard molecular dynamics (MD) simulations in conjunction with the molecular-mechanics Poisson-Boltzmann surface area (MM-PBSA) method to identify the critical residues involved in the complex formation. Further, we conducted MD simulations of nsp16/SAM, elucidating the

importance of nsp10 in the binding of SAM to nsp16. The detailed structural analysis and inter-molecular interactions reveal the interface of nsp16/nsp10, which provides a distinctive feature for coronaviruses, can be exploited as an attractive target in developing specific antiviral drugs for controlling COVID-19. MD simulations were conducted to elucidate the role of nsp10 in the interaction of SAM to nsp16. Also, the conformational changes in nsp10 and nsp16 due to their association were investigated.

## MATERIALS AND METHODS

We retrieved the experimental coordinate of the SARS-CoV-2 nsp16/nsp10 complex from Protein Data Bank (PDB), which was crystallized at 1.8 Å (PDB ID 6W4H) (Minasov et al., 2020). The complex structure includes S-adenosyl-L-methionine (SAM). The protonation states were determined using PROPKA 3.1 (Olsson et al., 2011), and the corresponding residues were modified accordingly. The following three systems were simulated for the current study: complex (nsp16/nsp10/SAM), nsp16<sub>SAM</sub> (nsp16/SAM), and nsp10<sub>apo</sub> (apo nsp10). The starting configurations of nsp16<sub>SAM</sub> and nsp10<sub>apo</sub> were constructed manually from nsp16/nsp10/SAM (PDB: 6W4H).

Missing hydrogens in the crystal structure were built using the *Leap* module of AmberTools19 (Case et al., 2018), and a proper amount of Na<sup>+</sup> was added to neutralize the system. All the systems were solvated in a periodic octahedron TIP3P water box (Price and Brooks, 2004) with a 10 Å buffering distance from all directions. The proteins (nsp10 and nsp16) were assigned the Amber ff14SB force field parameters (Maier et al., 2015) while the cofactor SAM was modeled using the updated Generalized Amber Force Field (GAFF2) (Wang et al., 2004) and AM1-bcc (Jakalian et al., 2002) charges. The bond lengths having hydrogen atoms were kept fixed using the SHAKE algorithm (Kräutler et al., 2001), which allowed 2 fs time-step for MD simulations. The Particle-Mesh Ewald (PME) summation (Darden et al., 1993) scheme was employed to compute the long-range interactions. The non-bonded cut-off was set to 10 Å.

Firstly, the solvated systems were subjected to an energy minimization using 500 steps of steepest descent, followed by another 500 steps of the conjugant gradient algorithm. During the minimization, the solute atoms were kept fixed with a restraint force of 2.0 kcal mol<sup>-1</sup>Å<sup>-2</sup>. The second stage of minimization was carried out without any restraint force. After the minimization, each system was gradually heated from 0 to 300 K in the NVT ensemble, and the solute atoms were restrained with force constant of 2.0 kcal mol<sup>-1</sup>Å<sup>-2</sup>. The temperature was maintained using a Langevin thermostat (Pastor et al., 1988; Loncharich et al., 1992). Subsequently, each system was simulated for 50 ps at 300 K at a constant pressure of 1 atm using the Berendsen barostat (Berendsen et al., 1984). In this stage also, the same restraint force was applied to the solute atoms. Before the production run, we equilibrated each system by conducting 1 ns MD simulation in the NPT ensemble without restraining the system. Finally, the production simulation was carried out for 1 μs using the *pmemd.cuda* module of AMBER18. Overall, 100,000

snapshots were generated and used for the analysis using the *Cpptraj* module (Roe and Cheatham, 2013) of AMBER18 (Case et al., 2018).

To study the effect of salt concentration on the binding, we simulated the complex system at 300 K for 1 μs at two different salt concentrations (0.15 and 0.25 M). The desired salt concentration was achieved by adding an appropriate number of monovalent ions (Na<sup>+</sup> and Cl<sup>-</sup>) obtained with the protocol suggested by Machado and Pantano (2020). Similarly, we have also investigated the effect of temperature on the binding by conducting MD simulation of the complex at a relatively elevated temperature of 310 K.

## Trajectory Analysis

All analyses, including root-mean-square deviations (RMSDs), root-mean-square fluctuations (RMSFs), radius of gyration (R<sub>g</sub>), solvent accessible surface area (SASA), etc. were performed using the *Cpptraj* module (Roe and Cheatham, 2013) of AMBER18. A distance of ≤ 3.5 Å and an angle cut-off of ≥ 120° were used for hydrogen bond calculations. The same criterion was used in earlier studies (Jeffrey, 1997; Hu et al., 2016; Shi et al., 2018; Sanachai et al., 2020).

## Principal Component Analysis

One of the widely used unsupervised data reduction schemes is principal component analysis (PCA) (Ichiye and Karplus, 1991). First, a covariance matrix (C) is constructed from the atomic fluctuations of C<sub>α</sub>-atoms of each residue (Amadei et al., 1996). The elements C<sub>ij</sub> of the covariance matrix C are defines as

$$C_{ij} = \langle (x_i - \langle x_i \rangle) (x_j - \langle x_j \rangle) \rangle \quad (1)$$

where  $x_i$  and  $x_j$  denotes the instant coordinates of the  $i$ th or  $j$ th atoms, while  $\langle x_i \rangle$  and  $\langle x_j \rangle$  denote the mean of  $i$ th or  $j$ th atoms over the ensemble. The diagonalization of the covariance matrix yields orthogonal eigenvectors and the corresponding eigenvalues. The resulting eigenvectors are termed as principal components (PCs) and indicate the direction of the movement, while the corresponding eigenvalue describes the amplitude of motions. We adopted the same methodology for PCA, as discussed in our earlier studies (Jonniya et al., 2019; Sk et al., 2020c).

The free energy landscape (FEL) was generated based on the following Equation (Frauenfelder et al., 1991):

$$G_i = -k_B T \ln \left( \frac{N_i}{N_m} \right) \quad (2)$$

where  $k_B$  represents the Boltzmann constant, and  $T$  is the absolute temperature.  $N_i$  is the population of the  $i$ th bin, and  $N_m$  is the population of the most populated bin. The 2-dimensional FEL was constructed using PC1 and PC2 as the reaction coordinate.

## Residual Network Analysis of Protein

The residual network analysis approach is widely used to explore the viral fitness and resistance development of protein structure. The network analysis of protein structures (NAPS) (Chakrabarty



et al., 2019) server (<http://bioinf.iit.ac.in/NAPS/>) was used to identify key residue interactions in the residual network and the network-based hydrophobic contacts from the simulation trajectories. Here, we used the protein-protein complex option, followed by the  $C_\alpha$  network type and unweighted edge weight. An edge represented the distance between a pair of  $C_\alpha$  atoms within the lower and upper thresholds (default upper threshold = 7 Å; lower threshold = 0 Å). We considered the default parameters for the long-range interaction networks and minimum residue separation of 1. The hydrophobicity indices of 20 amino acids range from -4.5 to 4.5 (Kyte and Doolittle, 1982). These values were colored in gradients of red to show the hydrophobic residues, while the gradients of blue were used to display the hydrophilic residues.

## Binding Free Energy and Alanine Scanning

The interaction energy between nsp10 and nsp16, and between the cofactor SAM and nsp16 in its both monomer and the complex were computed using the molecular mechanics Poisson-Boltzmann surface area (MM-PBSA) methodology (Kollman et al., 2000; Wang et al., 2006; Kar et al., 2007a,b, 2011, 2013; Hou et al., 2011). MMPBSA.py script available in the AmberTools19 was used for the analysis. Details of the MM-PBSA protocol were provided in our previous studies (Kar and Knecht, 2012a,b,c,d; Kar et al., 2013; Jonniya et al., 2019; Jonniya and Kar, 2020; Roy et al., 2020; Sk et al., 2020a,d), and the same protocol was adopted here.

The binding free energy is estimated by using the following equations of the MM-PBSA scheme:

$$\Delta G_{\text{bind}} = \Delta H - T\Delta S \approx \Delta E_{\text{internal}} + \Delta G_{\text{solv}} - T\Delta S \quad (3)$$

$$\Delta E_{\text{internal}} = \Delta E_{\text{covalent}} + \Delta E_{\text{elec}} + \Delta E_{\text{vdW}} \quad (4)$$

$$\Delta G_{\text{solv}} = \Delta G_{\text{pol}} + \Delta G_{\text{np}} \quad (5)$$

where  $\Delta E_{\text{internal}}$ ,  $\Delta G_{\text{solv}}$ , and  $T\Delta S$  represent the total internal energy, desolvation free energy, and conformational entropy, respectively. Further, the internal energy is composed of  $\Delta E_{\text{covalent}}$  (bond, dihedral, and angle),  $\Delta E_{\text{elec}}$  (electrostatic) and  $\Delta E_{\text{vdW}}$  (van der Waals) and the desolvation free energy is composed of polar ( $\Delta G_{\text{pol}}$ ) and non-polar solvation energies ( $\Delta G_{\text{np}}$ ). Here,  $\Delta G_{\text{pol}}$  was estimated from the Poisson-Boltzmann (PB) equation. The dielectric constant of the solute and solvent was set to 1.0 and 80.0, respectively.  $\Delta G_{\text{np}}$  was estimated from the following Equation (6),

$$\Delta G_{\text{np}} = \gamma (\text{SASA}) + b \quad (6)$$

Here, SASA represented the solvent-accessible surface area and was estimated using the LCPO (linear combination of pairwise overlap) algorithm (Weiser et al., 1999) with a probe radius of 1.4 Å. The surface tension coefficient,  $\gamma$  and offset ( $b$ ) value were set to 0.00542 kcal.mol<sup>-1</sup>.Å<sup>-2</sup> and 0.92 kcal.mol<sup>-1</sup>, respectively (Gohlke et al., 2003). For the MM-PBSA calculation, 2000 snapshots selected from the last 300 ns trajectory with a frequency of 15 ps were employed.

The configurational entropy was calculated using the normal mode analysis (NMA) method (Karplus and Kushick, 1981;

Rempe and Jónsson, 1998; Xu et al., 2011), and ~300 snapshots were used in the calculation due to high computational cost. Each configuration was energy minimized in an implicit solvent (nmode\_igb = 1) using a maximum of 50,000 steps, and a target root-mean-square gradient of 10<sup>-4</sup> kcal mol<sup>-1</sup>.Å<sup>-1</sup> via *mmpbsa\_py\_nabnmode* (Hawkins et al., 1995, 1996; Kar and Knecht, 2012a,b,c; Kar et al., 2013). NMA was applied to calculate the vibrational entropy ( $S_{\text{vib}}$ ) using the following equation (Carlsson and Åqvist, 2006);

$$S_{\text{vib}} = R \left[ \frac{x}{(e^x - 1)} - \ln(1 - e^{-x}) \right]; x = \frac{h\nu}{kT} \quad (7)$$

Where  $R$  denotes the universal gas constant,  $k$  is the Boltzmann constant, and  $T$  is the absolute temperature. The Planck constant and the vibrational frequency are denoted as  $h$  and  $\nu$ , respectively.

Further, the decomposition of the total binding free energy at the residue level was conducted by using the Molecular Mechanics Generalized Born Surface Area (MM-GBSA) scheme (Kar and Knecht, 2012a,b,c; Kar et al., 2013; Jonniya and Kar, 2020) as per the following equation.

$$\Delta G_{\text{residue}} = \Delta E_{\text{vdW}} + \Delta E_{\text{ele}} + \Delta \nu G_{\text{pol}} + \Delta G_{\text{np}} \quad (8)$$

The total contribution from each residue can also be defined as the sum of van der Waals ( $\Delta E_{\text{vdW}}$ ), electrostatic ( $\Delta E_{\text{ele}}$ ), polar ( $\Delta G_{\text{pol}}$ ), and non-polar ( $\Delta G_{\text{np}}$ ) terms. This method was proposed by Gohlke et al. (2003).

Finally, the Computational Alanine Scanning (CAS) was performed for some essential residues. This method yields the energy difference between the wild type and mutant (alanine) variants.

$$\Delta \Delta G_{\text{bind}} = \Delta G_{\text{mutant}} - \Delta G_{\text{wild}} \quad (9)$$

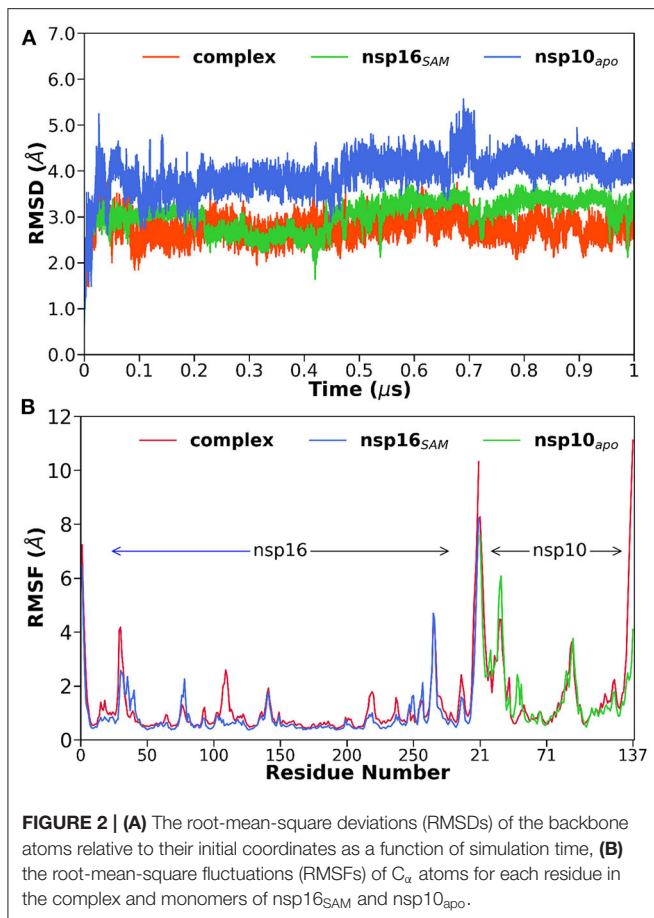
The basic principle involves in AS (alanine scanning) is the substitution of a residue with alanine that has an impact on the side-chain beyond  $C_\beta$  and not in the main-chain. *In vitro*, AS has been proven an advantageous mutagenesis method in finding hotspot residues in protein-protein interfaces. CAS is an excellent alternative approach to the *in vitro* experimental alanine scanning (Massova and Kollman, 1999; Moreira et al., 2007). Therefore, in this study, CAS was applied to illustrate further the importance of specific residues except alanine mentioned in the binding decomposition free energy of nsp16 of COVID-19.

## RESULTS AND DISCUSSION

To explore the mechanism underlying the dimerization of nsp16 and nsp10 as well as the preferential binding of the cofactor SAM to the nsp16/nsp10 heterodimer compared to nsp16 (nsp16<sub>SAM</sub>), a conformational free energy landscape (FEL) and binding free energy calculations were performed using the MD/MM-PBSA scheme.

### Overall Structural Dynamic Features

To explore the thermodynamic stability of each system and to ensure the rationality of the sampling method, we monitored



the structural and energetic properties during the entire 1  $\mu$ s production simulation. The time evolution of the root-mean-square deviations (RMSDs) of the protein backbone atoms, which reflects the stability of the system, were calculated relative to the initial configuration and shown in **Figure 2A**. It is worth mentioning here that a stable RMSD does not always provide stable energy profiles; hence we have also verified the potential and total energy of each system from the respective MD trajectory (data not shown).

The RMSD plots indicated that all the studied systems reached equilibrium after  $\sim$ 100 ns. The average RMSD value varies between 2.8 and 4.0  $\text{\AA}$  for all systems (see **Table 1**). The highest and lowest deviations were obtained for nsp10<sub>apo</sub> and complex, respectively. An intermediate RMSD value of 3.1  $\text{\AA}$  was obtained for nsp16<sub>SAM</sub>. Overall, the nsp16/nsp10/SAM complex showed more stability throughout the simulations than nsp16<sub>SAM</sub> or nsp10<sub>apo</sub>. This suggests that the dimerization leads to the overall stabilization of the complex.

Moreover, we also calculated the temporal RMSDs of heavy atoms of the cofactor SAM (see **Supplementary Figure 1A**) and the backbone atoms of residues within 5  $\text{\AA}$  around SAM in the binding pocket (see **Supplementary Figure 1B**). It is evident from **Supplementary Figure 1B** that the RMSD values of SAM and the binding pocket for the complex were stable up to

**TABLE 1 |** The average value of protein backbone RMSD and solvent-accessible surface area (SASA) obtained from MD simulations.

System	RMSD ( $\text{\AA}$ )	SASA ( $\text{\AA}^2$ )
Complex	2.8 (0.1)	18928.1 (103.3)
nsp16 <sub>SAM</sub>	3.1 (0.3)	13467.3 (140.2)
nsp10 <sub>apo</sub>	4.0 (0.2)	6663.8 (145.7)

Standard deviations are given in parentheses.

850 ns of the simulation. After that, in the last 150 ns, a sudden increase in RMSD was observed. Overall, the average RMSD value was 0.7  $\text{\AA}$  and 0.8  $\text{\AA}$  for SAM and the binding pocket, respectively (see **Supplementary Table 1**). It indicates that SAM binds strongly onto the cofactor binding cavity of the heterodimer nsp16/nsp10. However, in the case of nsp16<sub>SAM</sub>, the RMSD values of SAM and the binding cavity were relatively stable up to 100 ns. After that, the RMSD value increased by  $\sim$ 3 times compared to the complex system (see **Supplementary Table 1** and **Supplementary Figure 1**). These high values of RMSDs suggest that SAM does not bind to nsp16 monomer (nsp16<sub>SAM</sub>), which is in agreement with the experimental study by Chen and coworkers for SARS-CoV (Chen et al., 2011).

Additionally, three loops, namely 71–79, 100–108, and 130–148, which comprises the SAM binding pocket as shown in the crystal structure, were also analyzed and found to be stable for both complex and nsp16<sub>SAM</sub> (see **Supplementary Figures 2A–C**). However, the cap-binding groove of nsp16 in SARS-CoV, as well as SARS-CoV-2, is mainly composed of two flexible loops, comprised of residues 26–38 and 130–148, while in the case of flavivirus, the NS5 MTase was relatively stable with  $\alpha$ -helices (A1, A2, and half of  $\alpha$ D) along the cap-binding groove (Egloff et al., 2002). Among the two loops involved in the cap-binding, only the loop 26–38 exhibited differences in the complex and nsp16<sub>SAM</sub> system, as revealed from our simulations. The 26–38 loop is located near the interface of nsp16 and nsp10. On the other hand, the 130–148 loop is found near the SAM binding pocket, away from the nsp16/nsp10 interface. As shown in **Supplementary Table 1**, the average RMSD value of this loop was higher in nsp16<sub>SAM</sub> (3.1  $\text{\AA}$ ) compared to the complex (1.4  $\text{\AA}$ ). The time evolution of RMSD of the 26–38 loop and the corresponding potential mean force (PMF) were displayed in **Supplementary Figures 3A,B**. From **Supplementary Figure 3A**, it was observed that in the case of nsp16<sub>SAM</sub>, the RMSD value of the loop 26–38 increased during the initial 300 ns and remained stable thereafter. On the other hand, in the complex case, the RMSD of the loop was found to increase during the initial 300 ns and gradually decreased up to 600 ns of the simulation and finally reached equilibrium. We computed the potential of mean force (PMF), taking the loop's RMSD as a reaction coordinate and shown in **Supplementary Figure 3B**. The primary low energy structure of the loop was observed at  $\sim$ 3.2  $\text{\AA}$  for nsp16<sub>SAM</sub>. However, for the complex system, the global energy minimum was found at a relatively lower RMSD (1.4  $\text{\AA}$ ). Besides, we detected two secondary minima ( $\sim$ 1.9  $\text{\AA}$ , and  $\sim$ 2.8  $\text{\AA}$ ) for the 26–38 loop in

the complex system, and the energy barriers of the adjacent states were  $\sim 1.1$  and  $1.2$  kcal/mol, respectively. Overall, our results suggest that the dimerization resulted in the loop rearrangement near the interface.

Next, we measured the root-mean-square fluctuations (RMSFs) of C $\alpha$  atoms for all systems (see **Figure 2B**) to elucidate the effect of dimerization on the residual flexibility. It is evident from **Figure 2B** that all three systems displayed a similar trend in RMSF patterns. However, we found some dynamic fluctuations in different loop regions, including the N- and C-terminals. A relatively large fluctuation was observed for various loop regions located at residues 26–38, 74–80, 104–115, and 130–148. The loop regions 26–38 and 104–115, which contribute to the interface of the heterodimer, showed higher fluctuations in complex compared to nsp16<sub>SAM</sub>, which suggests that the dimerization leads to the loop rearrangements. In contrast, the 74–80 loop region, located near SAM binding pocket, stabilized after the heterodimerization. However, the cap-binding groove of the 130–148 loop region exhibited no differences in both complex and apo forms, which agrees with the RMSD analysis (**Supplementary Figure 2C**). Overall, it depicts the binding of nsp10 to nsp16 favors and stabilizes the binding pocket of SAM, leading to its high activity.

Finally, we also measured the solvent-accessible surface area (SASA) of all systems and reported in **Table 1**. The average SASA values were found to be 18928.1, 13467.3, and 6663.8 Å<sup>2</sup>, for the complex, nsp16<sub>SAM</sub>, and nsp10<sub>apo</sub>, respectively. This suggested that the dimerization of nsp16 and nsp10 covered  $\sim 1,203$  Å<sup>2</sup> surface area in total, indicating a very stable interaction. Our simulation results also favor an experimental study that showed the value of the solvent-exposed surface area for the heterodimer complex of nsp16/nsp10 as 19710 Å<sup>2</sup> (Rosas-Lemus et al., 2020).

## Free Energy Landscape (FEL) of SAM Binding

The RMSD profile of SAM and the binding pocket (**Supplementary Figure 1**) for the complex and nsp16<sub>SAM</sub> systems suggested that SAM binds more strongly to the heterodimer nsp16/nsp10 than the monomer nsp16. The 2-dimensional free energy landscape (FEL) was generated for the complex and nsp16<sub>SAM</sub> systems to explore the strong and weakly bound states of the SAM molecule. The RMSD of heavy atoms of SAM and the center of mass (CoM) distance between SAM and nsp16, which characterizes the displacement of SAM from the substrate-binding pocket of nsp16, were used as reaction coordinates for the construction of FEL. The value of a CoM distance  $< 14.5$  Å denotes the strong binding of SAM toward nsp16. The two-dimensional FEL of the complex (nsp16/nsp10/SAM) and monomer (nsp16<sub>SAM</sub>) systems were shown in **Figures 3A,B**, and the corresponding positions of SAM in the binding cavity were depicted in **Figures 3C,D**. FEL of the complex and monomer systems suggested that the conformational state of SAM in two systems prefer disparate configurations. In the case of the heterodimeric complex system, the underlying FEL was characterized by a single global minimum (see **Figure 3A**), which corresponds to the strongly

bound state of SAM. On the other hand, in the case of nsp16<sub>SAM</sub>, the global free energy minimum was obtained at a CoM distance of  $\sim 17.5$  Å, which corresponds to a weakly or unbound state of SAM. The secondary minimum was detected at a CoM distance of  $\sim 13.5$  Å, which corresponds to a strongly bound state of SAM to nsp16<sub>SAM</sub>. Overall, our results suggested that although nsp16 monomer (nsp16<sub>SAM</sub>) favored two binding states, the weakly bound or unbound state is energetically more favorable than the strongly bound state. These results illustrated a stronger binding of SAM with the nsp16/nsp10 heterodimer than nsp16 alone (nsp16<sub>SAM</sub>), which agrees with the experimental results obtained for SARS-CoV (Chen et al., 2011).

## Principal Component Analysis of nsp16/nsp10

The principal component analysis (PCA) was carried out for both nsp16 and nsp10 when they are in complex and monomeric states. FELs of sub-units nsp16 (nsp16<sub>complex</sub>) and nsp10 (nsp10<sub>complex</sub>) in the complex were compared with the corresponding monomer simulations (nsp16<sub>SAM</sub> and nsp10<sub>apo</sub>). Each eigenvector and eigenvalue was plotted in the decreasing order, as shown in **Supplementary Figure 4**. For all cases, the first few eigenvectors describe the collective motion of local fluctuations. Comparing the four systems indicated that the first few PCs that describe the properties of movements were not the same. The first two eigenvectors encapsulated for 42, 67, 46, and 70% of overall movements in nsp16<sub>complex</sub> (nsp16 in complex), nsp10<sub>complex</sub> (nsp10 in complex), nsp16<sub>SAM</sub>, and nsp10<sub>apo</sub>, respectively. Similarly, the first ten eigenvectors accounted for 80–90% of the total motions in all four systems.

Next, we constructed the 2-dimensional FEL at 300 K for each system using the first two principal components (PC1 and PC2) as reaction coordinates and shown in **Figures 4A–D**. The sampling space of four systems was different, as evident from **Figure 4**. The conformational sampling space of nsp16<sub>complex</sub> (nsp16 in nsp16/nsp10/SAM), depicted in **Figure 4A**, was found to be restricted compared to the other three systems, which sampled more expansive conformational space. From **Figure 4A**, we observed a global minimum of 62.7% occupancy and a secondary minimum of 37.3% occupancy, which suggested that the nsp16<sub>complex</sub> system is more stabilized in the presence of nsp10. In the monomeric form of nsp16<sub>SAM</sub>, a wider conformational basin was sampled (see **Figure 4C**), and the energy barriers between adjacent minima were  $\sim 1.5$  kcal/mol. On the other hand, nsp10 sampled more phase space than nsp16 in the complex as well in its monomer apo form, as shown in **Figures 4B,D**. However, nsp10<sub>apo</sub> has three distinct conformations with an energy barrier of 4.0 kcal/mol suggesting structural disparity in both nsp10<sub>complex</sub> and nsp10<sub>apo</sub> as compared to nsp16.

## Residual Network Analysis

The Network Analysis of Protein Structure (NAPS) server provided a visual examination of sub-network based on the physicochemical properties of the protein residues to find more details about the interaction between nsp16 and nsp10 (see



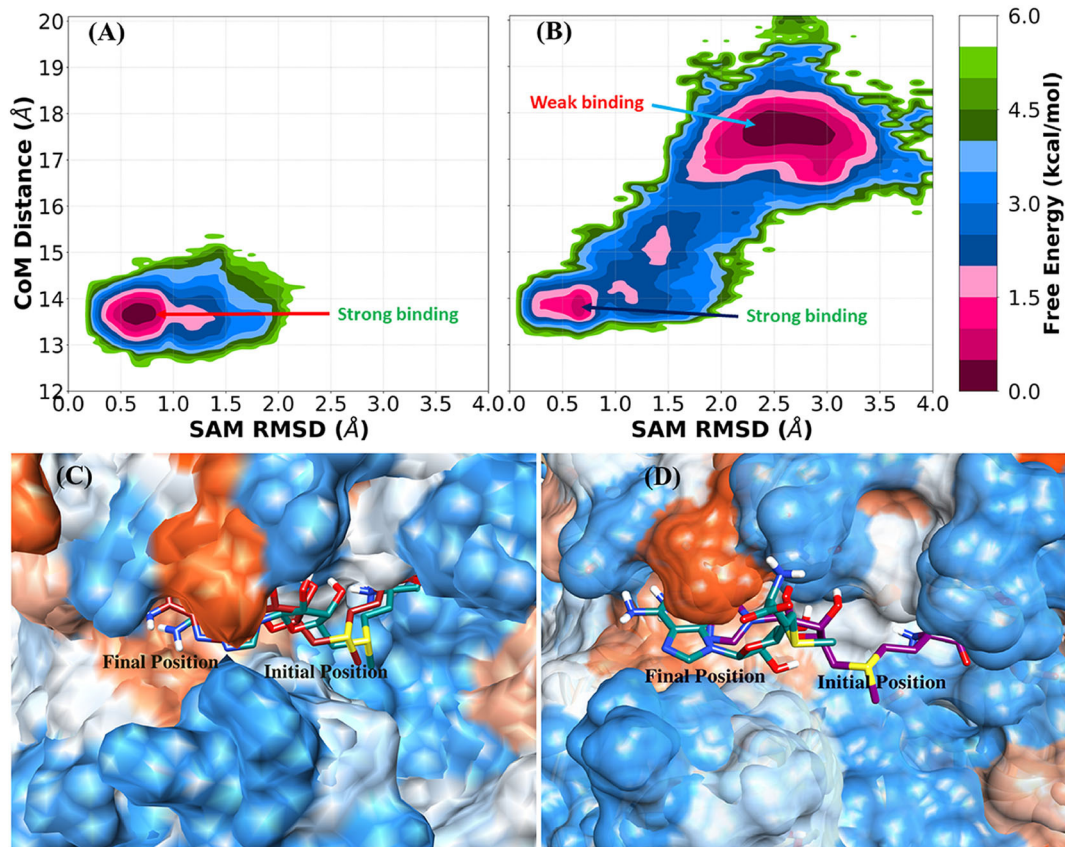


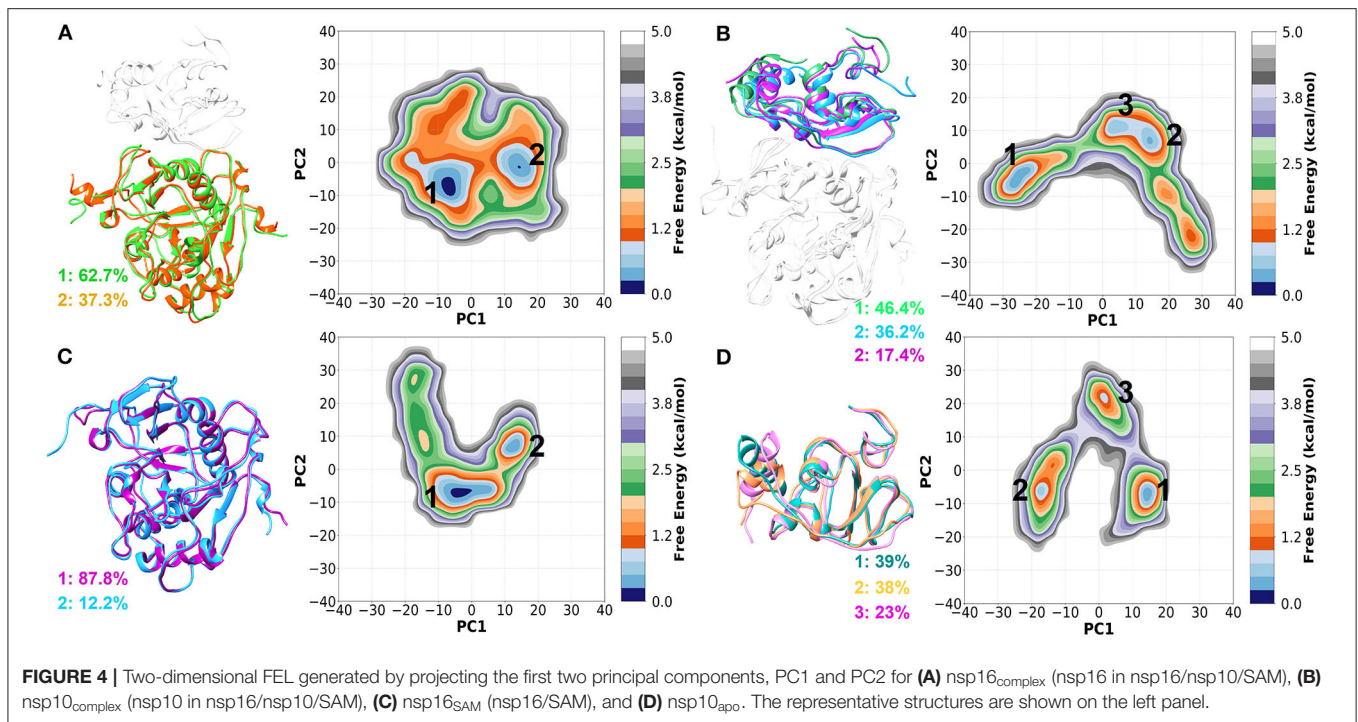
**FIGURE 3** | Free energy landscape (FEL) and representative SAM position in the complex (nsp16/nsp10/SAM) and nsp16<sub>SAM</sub> (nsp16/SAM). **(A)** FEL of SAM bound with nsp16 in the complex, **(B)** FEL of SAM bound with monomer nsp16<sub>SAM</sub>. Representative structures of **(C)** SAM with nsp16 in the complex and **(D)** SAM with monomer nsp16<sub>SAM</sub>.

**Figure 5**). Herein, we explored the 3D interaction network of hydrophobic residues of nsp16 and nsp10. The results showed that the number of hydrophobic interaction networks between nsp16 and nsp10 was initially very high, and after 100 ns, the number of networks reduced to  $\sim 2-3$ . The hydrophobic interaction networks, such as (V104, A71) and (P80, V42), were found as strong and stable contacts throughout the simulation time (see **Supplementary Table 2**). We also calculated the total number of interactions and noticed that the number of interaction networks was more or less conserved throughout the first 500 ns (see **Supplementary Figure 5**). In general, it can be concluded from our analyses that nsp16 and nsp10 interact with a very high affinity.

### Binding Free Energy of SAM Bound to nsp16/nsp10 Heterodimer and nsp16 Alone

The differences in binding affinity of the SAM molecule toward nsp16 alone (nsp16<sub>SAM</sub>) and nsp16/nsp10 heterodimer (complex) were calculated by utilizing the MM-PBSA scheme. The MM-PBSA scheme provides various components contributing to the total binding energy ( $\Delta G_{\text{bind}}$ ), such as van der Waals interactions ( $\Delta E_{\text{vdW}}$ ), electrostatic interactions ( $\Delta E_{\text{ele}}$ ), polar solvation energy ( $\Delta G_{\text{pol}}$ ), non-polar solvation free

energy ( $\Delta G_{\text{np}}$ ), and configurational entropy ( $T\Delta S$ ). All these components of the binding free energy of SAM to nsp16<sub>SAM</sub> or nsp16/nsp10 (complex) were shown in **Table 2**. The binding free energy of SAM to the heterodimer nsp16/nsp10 was estimated as  $-6.8 (\pm 0.9)$  kcal/mol, which agrees with the experimental result ( $-7.4 \pm 0.1$  kcal/mol) (Lin S. et al., 2020). On the other hand, SAM was found to bind very weakly ( $\Delta G_{\text{bind}} = -0.6 \pm 0.8$  kcal/mol) to nsp16 monomer (nsp16<sub>SAM</sub>), as evident from **Table 2**. This is consistent with **Figures 3A,B**. A similar mode of SAM binding was observed for SARS-CoV nsp16/nsp10 or nsp16 alone. For both cases, the intermolecular van der Waals interactions ( $\Delta E_{\text{vdW}}$ ), electrostatic interactions ( $\Delta E_{\text{ele}}$ ), and non-polar solvation free energy ( $\Delta G_{\text{np}}$ ) favored the binding of SAM. In contrast, polar solvation energy ( $\Delta G_{\text{pol}}$ ) and entropy ( $T\Delta S$ ) disfavored the complexation. The electrostatic interaction energy was more favorable than the van der Waals interactions for both cases. In nsp16<sub>SAM</sub>, although  $\Delta E_{\text{ele}}$  was much more favorable ( $-76.8$  kcal/mol) than  $\Delta E_{\text{vdW}}$  ( $-28.6$  kcal/mol). However, the disfavorable polar solvation energy ( $\Delta G_{\text{pol}} = 84.7$  kcal/mol) overcompensated the intermolecular electrostatic interaction energy. Hence, the overall polar contribution ( $\Delta E_{\text{ele}} + \Delta G_{\text{pol}}$ ) was found to be unfavorable (7.9 kcal/mol) to the SAM binding. In contrast, the overall non-polar contribution



( $\Delta E_{vdW} + \Delta G_{np}$ ) was found to be  $-32.1$  kcal/mol. It implies that hydrophobic interactions drive the binding. In the case of the complex system (nsp16/nsp10/SAM), the binding affinity of SAM to nsp16 increases, as evident from **Table 2**. Here, the electrostatic interactions energy ( $\Delta E_{ele} = -181.1$  kcal/mol) was more favorable than the van der Waals energy ( $\Delta E_{vdW} = -40.4$  kcal/mol). The total polar contributions ( $\Delta E_{ele} + \Delta G_{pol}$ ) value was found to be favorable ( $-2.1$  kcal/mol) to the binding of SAM, which is in contrast to what had been observed for nsp16<sub>SAM</sub>. Further, the overall polar energy was less favorable than the net non-polar contribution ( $\Delta E_{vdW} + \Delta G_{np} = -44.5$  kcal/mol). Hence, in the complex, the main force behind the binding of SAM to nsp16 is hydrophobic interactions. Overall, the binding free energy analysis showed that the binding affinity of the SAM molecule to nsp16 increases with the presence of nsp10. This implies that nsp10 acts as a stimulator to bind SAM to nsp16/nsp10 of SARS-CoV-2, which agrees with the experiment (Viswanathan et al., 2020). Wang and coworkers obtained a similar result for SARS-CoV and MERS-CoV (Wang et al., 2015).

Further, to explore the significant residues of nsp16 in the binding of SAM and to evaluate the differences in the complex (nsp16/nsp10) and monomer (nsp16<sub>SAM</sub>), the per-residue decomposition of the binding free energy was performed using the MM-GBSA approach. All the residues having  $> 1.5$  kcal/mol of energetic contributions were considered important and shown in **Figure 6**. As seen in **Table 3**, the number of amino acids contributing to binding with SAM is high in the complex as compared to nsp16<sub>SAM</sub>. Residues such as Leu100, Asp99, Cys115, Met131, Phe149, and Asp114 are common in cases of complex and nsp16<sub>SAM</sub>. Apart from these residues,

additional residues, such as Asn43, Tyr47, Gly71, Tyr132, and Ser74, also played a significant role in the binding of SAM to the complex heterodimer. These results are consistent with the higher binding affinity of SAM in the complex than the nsp16 monomer. All these residues were also considered as SAM-engaging in an experimental study by Lin S. et al. (2020). It is worth noting here that all these SAM-interacting residues are conserved both in SARS-CoV and MERS-CoV, suggesting a conserved binding mode of SAM in these viruses. The conserved SAM-binding mechanism to nsp16/nsp10 also opens the possibility of developing a pan-CoV inhibitor by targeting this SAM-binding pocket.

## Hydrogen Bond Interaction Between nsp16 and SAM

Next, we investigated the hydrogen bond (H-bond) interactions between SAM and nsp16 in the complex and apo forms (see **Table 4**). The % occupancy calculated from the respective MD trajectories reflected the stability of H-bonds. As seen in **Table 4**, residues with  $> 50\%$  H-bond occupancy in the MD simulations were recognized for the complex (nsp16/nsp10) compared to monomer nsp16<sub>SAM</sub>. The residues, including Asp130, Tyr47, Gly71, and Asp99, showed more H-bond stability in the complex. Overall, a stable H-bond is formed between nitrogen and oxygen atoms of SAM with Asp130, Tyr47, Gly71, and Asp99 residues of nsp16, respectively. Hence, the identified significant residues like Asp130, Tyr47, Gly71, and Asp99 of nsp16 may aid in the development of SAM competitive inhibitors.

The changes in the distance of the atoms forming H-bond between SAM and nsp16 were also determined and shown in **Supplementary Figure 6**. In the complex, the distance between



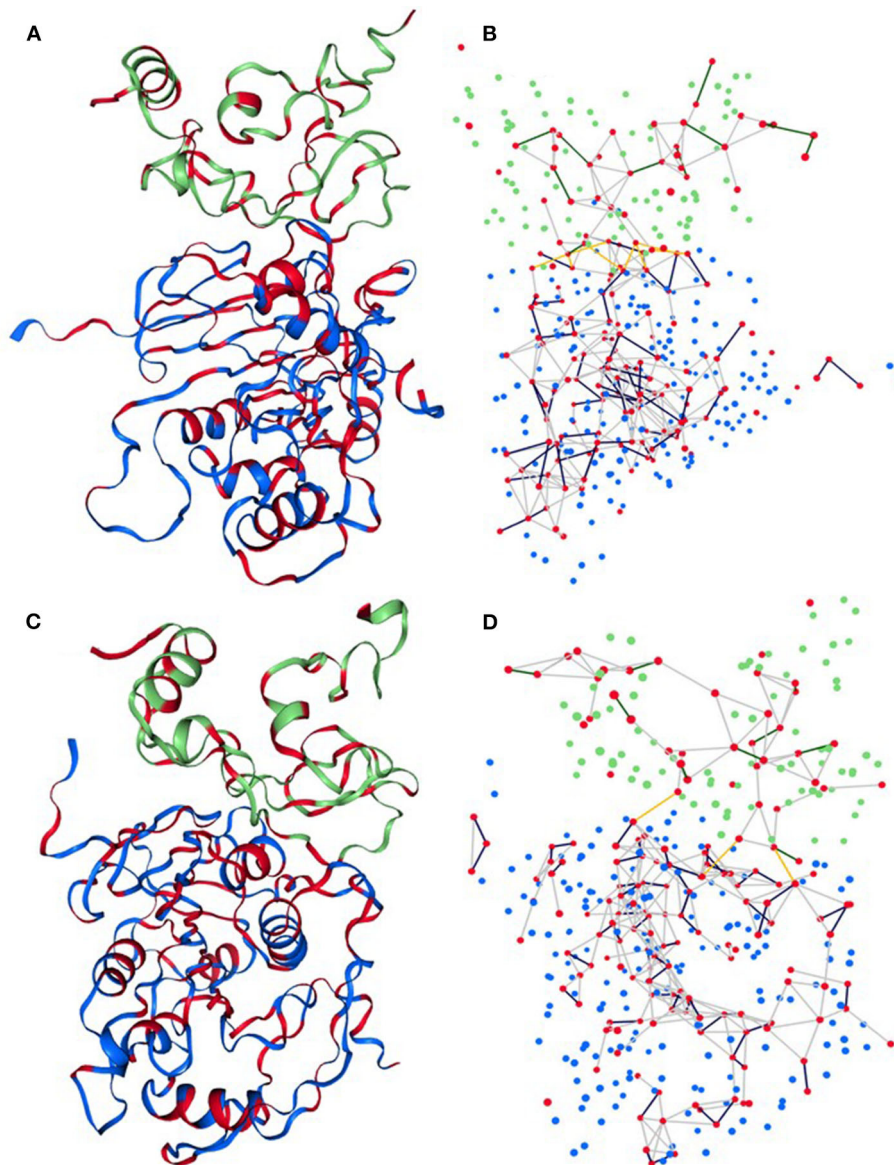


**FIGURE 5** | Sub-network representation of network 3D view of **(A,B)** initial structure and **(C,D)** final structure of the complex. Each residual  $C_{\alpha}$  atom is represented by a sphere where the red sphere indicates hydrophobic residues. Blue and green color spheres correspond to residues of nsp16 and nsp10, respectively. The yellow line edges represent the contact network of hydrophobic residues between nsp16 and nsp10.

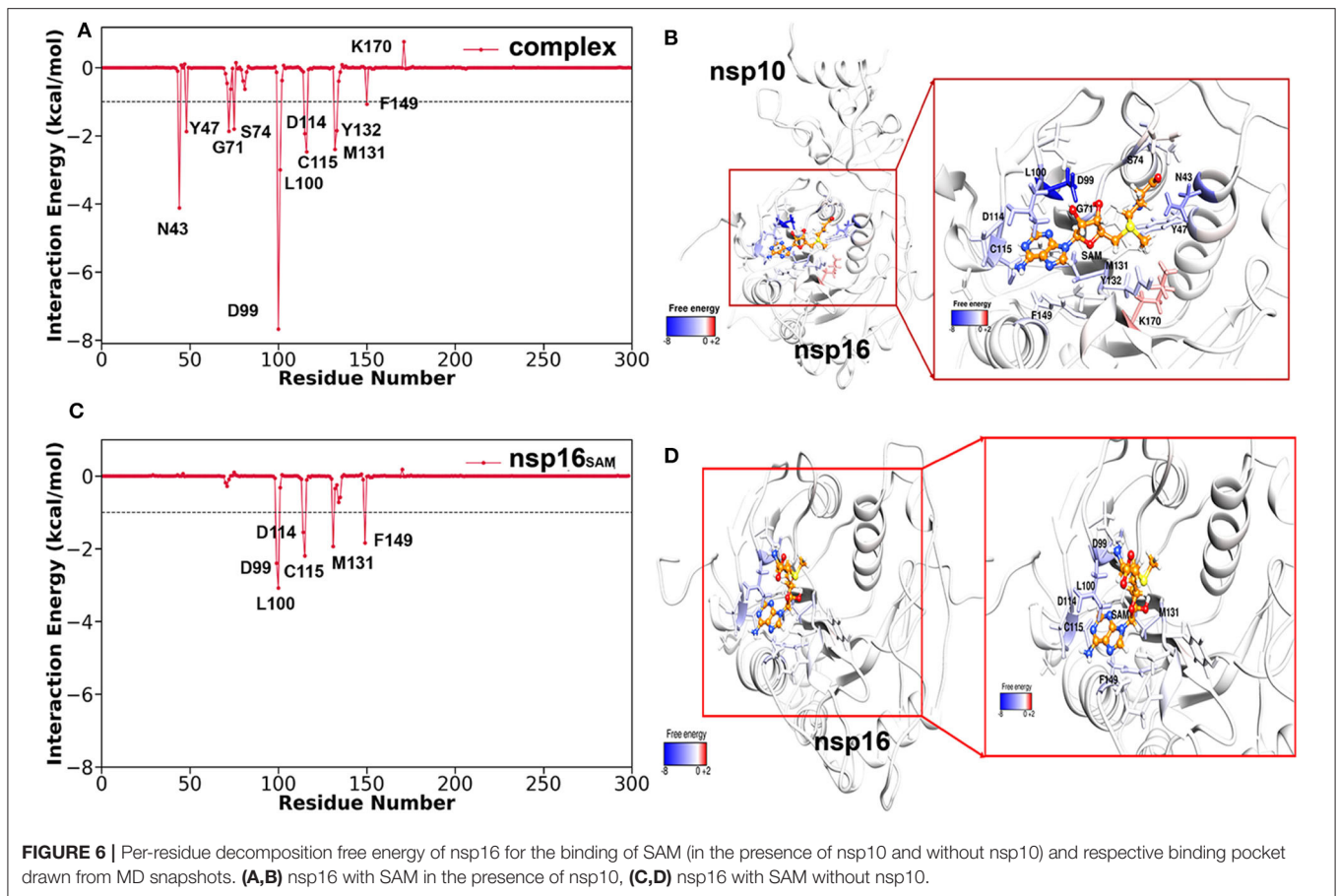
**TABLE 2** | Energetic components of the total binding free energy of SAM bound to the heterodimer nsp16/nsp10 (complex), and nsp16 alone (nsp16<sub>SAM</sub>).

System	$\Delta E_{vdw}$	$\Delta E_{elec}$	$\Delta G_{pol}$	$\Delta G_{np}$	$\Delta H$	$\Delta -TS$	$\Delta G_{bind}$
Complex	-40.4 (0.1)	-181.1 (0.5)	179.0 (0.4)	-4.1 (0.0)	-46.6 (0.2)	39.8 (0.9)	-6.8 (0.9)
nsp16 <sub>SAM</sub>	-28.6 (0.1)	-76.8 (0.6)	84.7 (0.6)	-3.5 (0.0)	-24.2 (0.1)	23.6 (0.8)	-0.6 (0.8)

All values are given in kcal/mol. The standard error of the mean is provided in parentheses.

the oxygen atom of Asp130, Tyr47, and Gly71 of nsp16 and the nitrogen atom of SAM illustrated the average distance of 3.01, 2.89, and 3.01 Å, respectively, suggesting strong H-bond interactions. In the case of nsp16<sub>SAM</sub>, the average distances

for these atoms were 12.48, 14.64, and 11.06 Å, respectively, indicating a lack of formation of H-bonds in the nsp16 monomer. However, for Asp99, the distance between its oxygen atom (OD1 and OD2) and the oxygen atom (O3) of SAM illustrated



an average distance of 2.9 Å and 3.2 Å for the complex and monomer, respectively. In contrast, the average distance between Asp99 (OD2) and SAM (O2) was higher for monomer (4.2 Å) than the complex (3.1 Å). All these results were consistent with the occupancy analysis. Further, they emphasized that Asp130, Tyr47, and Gly71 of nsp16 were key residues in the binding of SAM and for the 2'-O-MTase activity of nsp16.

### Energetics of nsp16/nsp10 Complexation

To evaluate further the binding free energy of the heterodimer (nsp16/nsp10),  $\Delta G_{\text{bind}}$  was estimated using the MD/MM-PBSA approach and reported in **Table 5**. From **Table 5**, the binding free energy ( $\Delta G_{\text{bind}}$ ) between nsp16 and nsp10 was found to be  $-47.4$  kcal/mol. The various components of the total binding free energy indicate that the intermolecular van der Waals interactions ( $\Delta E_{\text{vdW}}$ ), electrostatic interactions ( $\Delta E_{\text{ele}}$ ), and non-polar solvation free energy ( $\Delta G_{\text{np}}$ ) favors the binding of nsp10 and nsp16. While polar solvation free energy ( $\Delta G_{\text{pol}}$ ) disfavor the binding. The electrostatic interactions ( $\Delta E_{\text{ele}}$ ) energy is higher ( $-429.4$  kcal/mol) than the van der Waal interactions ( $\Delta E_{\text{vdW}}$ ) ( $-90.4$  kcal/mol) (see **Supplementary Figure 7**). However, the disfavoring components of polar solvation energy ( $\Delta G_{\text{pol}}$ ) compensate for the  $\Delta E_{\text{ele}}$  being a value of 481.7 kcal/mol. Hence, the total polar interactions ( $\Delta E_{\text{ele}} + \Delta G_{\text{pol}}$ ) disfavor the binding between nsp10 and nsp16 with a value of 52.3

kcal/mol. In contrast, the total non-polar contributions ( $\Delta E_{\text{vdW}} + \Delta G_{\text{np}}$ ) favor the binding between nsp16 and nsp10 ( $-100.0$  kcal/mol). Therefore, the binding between nsp10 and nsp16 is mainly driven by hydrophobic interactions. Overall, the binding free energy analysis depicts, the binding affinity of the SAM in the complex nsp16/nsp10 ( $\Delta G_{\text{bind}} = -46.6$  kcal/mol) is similar to that between nsp10 and nsp16 ( $\Delta G_{\text{bind}} = -47.4$  kcal/mol) of SARS-CoV-2. These observations were in agreement with its similar homology virus, SARS-CoV (2002). A similar binding affinity was seen between nsp10 and nsp16, as well as between SAM and the nsp16/nsp10 complex of SARS-CoV (Chen et al., 2011).

To further investigate the critical residues involved in the binding between nsp10 and nsp16, the binding free energy was decomposed at the individual residue level using the MM-GBSA approach and shown in **Figure 7**. Here, we considered only residues having the energy value  $\geq 1.0$  kcal/mol and listed in **Supplementary Table 3**. The key residues from nsp10 include Leu45, Ala71, Val42, Met44, Tyr96, Gly69, Thr47, Arg78, Gly70, Gly94, and Pro59. Similarly, the critical residues from nsp16 include Ile40, Val104, Ala83, Val78, Met247, Val44, Gln87, Arg86, Lys76, Lys38, Val84, and Met41. It indicates that hydrophobic interactions significantly control the binding between nsp10 and nsp16. Our findings agree with a recent experimental study (Lin S. et al., 2020) where it was reported that a total of 31

**TABLE 3** | Per-residue decomposition of the total binding free energy (kcal/mol) of SAM to the complex (nsp16/nsp10) and monomer (nsp16<sub>SAM</sub>) systems.

Residue	T <sub>vdw</sub>	T <sub>ele</sub>	T <sub>pol</sub>	T <sub>np</sub>	T <sub>back</sub>	T <sub>side</sub>	T <sub>total</sub>
<b>COMPLEX</b>							
Asp99	0.71	-29.08	20.84	-0.14	-0.73	-6.94	-7.67
Asn43	-0.01	-9.90	5.89	-0.12	-0.30	-3.84	-4.14
Leu100	-2.42	-0.19	-0.10	-0.28	-0.87	-2.12	-2.99
Cys115	-0.74	-2.01	0.33	-0.05	-1.21	-1.26	-2.47
Met131	-2.72	0.56	-0.12	-0.13	-0.47	-1.94	-2.41
Asp114	-0.30	-8.98	7.41	-0.07	-0.77	-1.17	-1.94
Tyr47	0.07	-5.46	3.56	-0.04	-0.01	-1.86	-1.87
Gly71	-1.35	-3.27	2.84	-0.08	-1.36	-0.50	-1.86
Tyr132	-2.15	-2.23	2.86	-0.32	-0.93	-0.91	-1.84
Ser74	-0.95	-4.31	3.54	-0.08	-0.45	-1.35	-1.80
Phe149	-1.20	0.12	0.12	-0.13	-0.16	-0.93	-1.09
<b>nsp16<sub>SAM</sub></b>							
Leu100	-3.04	1.61	-1.17	-0.47	-0.18	-2.89	-3.07
Asp99	0.62	-19.83	16.98	-0.16	-0.15	-2.24	-2.39
Cys115	-0.70	-1.73	0.30	-0.06	-1.16	-1.03	-2.19
Met131	-1.72	-0.02	-0.05	-0.15	-0.55	-1.39	-1.94
Phe149	-1.86	-0.33	0.54	-0.18	-0.20	-1.63	-1.83
Asp114	-0.28	-7.47	6.32	-0.10	-0.73	-0.80	-1.53

The van der Waals ( $T_{vdw}$ ), electrostatic interactions ( $T_{ele}$ ), polar ( $T_{pol}$ ), and non-polar solvation energy ( $T_{np}$ ) and the total residual energy ( $T_{total}$ ) are shown.  $T_{back}$  and  $T_{side}$  represent the backbone and side-chain parts, respectively.

residues (Asn40, Val42, Lys43, Met44, Leu45, Cys46, Thr47, Pro59, Gly70, Ala71, Cys77, Arg78, Lys93, Gly94, and Tyr96 in nsp10 and Lys38, Gly39, Ile40, Met41, Val44, Lys76, Val78, Pro80, Ala83, Arg86, Gln87, Val104, Ser105, Asp106, Leu244, and Met247 in nsp16) mediates the intimate nsp16-nsp10 interaction. The per-residue decomposition of the binding free energy was further validated by other computational approaches, such as FTmap (Kozakov et al., 2015). The final complex structure obtained from the MD trajectory was analyzed using FTmap, and Gln87, Arg86, Val104, Met247 of nsp16, and Leu45, Met44, Pro59, Arg78, Tyr96 of nsp10 were identified as the hotspot residues, which again agrees with the MM-GBSA analysis.

## Interaction Analysis Between nsp16 and nsp10

In the above finding of binding free energy analysis, we have seen that nsp10 acts as a stimulator in the binding of the SAM to nsp16. Hence, to further explore the binding interactions between nsp16 and nsp10, H-bond and hydrophobicity analysis was calculated. As seen in **Table 6**, the H-bond occupancy reflects the stability of H-bond formation between protein-protein in the MD simulations. The strong H-bonds were formed between residues Ala83 (nsp16) and Tyr96 (nsp10) and between Gln87 (nsp16) and Leu45 (nsp10). Other residues, including Asp106 (nsp16), formed two H-bonds with Ala71 and Gly94 of nsp10, Lys38 (nsp16) to Lys43 (nsp10), and Ser105 (nsp16) to Lys93 (nsp10). Hydrophobic interactions also played an important role

**TABLE 4** | Hydrogen bonds formed between SAM and receptor (nsp16/nsp10 or nsp16).

Binding couples		Molecular dynamics	
Acceptor	Donor...H	Distance (Å)	Occupancy <sup>a</sup> (%)
<b>COMPLEX</b>			
Asp130@OD2	SAM@N...HN1	2.84	71.69
SAM@N	Tyr47@OH...HH	2.79	64.95
Gly71@O	SAM@N...HN2	2.86	55.16
Asp99@OD2	SAM@O2'...HO2'	2.62	53.90
Asp99@OD1	SAM@O3'...HO3'	2.66	53.80
Asp99@OD2	SAM@O3'...HO3'	2.66	46.27
SAM@HN1	Tyr47@OH...HH	2.78	45.41
Asp99@OD1	SAM@O2'...HO2'	2.63	45.15
SAM@O	Asn43@ND2...HD22	2.84	42.20
SAM@OXT	Asn43@ND2...HD22	2.84	37.76
SAM@N1	Cys115@N...H	2.92	33.86
Asp114@OD2	SAM@N6...HN61	2.80	18.10
Asp114@OD1	SAM@N6...HN61	2.80	15.11
SAM@O2'	Asn101@ND2...HD22	2.89	12.21
<b>nsp16<sub>SAM</sub></b>			
Asp99@OD1	SAM@O3'...HO3'	2.64	48.80
Asp99@OD2	SAM@O3'...HO3'	2.63	45.78
SAM@N1	Cys115@N...H	2.92	28.66
Asp114@OD2	SAM@N6...HN61	2.80	26.44
Asp114@OD1	SAM@N6...HN61	2.80	24.80
Asp114@OD2	SAM@N6...HN62	2.80	19.03
Asp114@OD1	SAM@N6...HN62	2.80	17.95
Asp99@OD1	SAM@O2'...HO2'	2.65	16.42
Asp99@OD2	SAM@O2'...HO2'	2.65	14.70
SAM@N	Tyr47@OH...HH	2.92	11.31

<sup>a</sup>only H-bonds with more than 10% occupancy are listed.

The corresponding average distance and percentage occupancy are also provided.

**TABLE 5** | Energetic components of the dimerization energy ( $G_{bind}$ ) between nsp16 and nsp10.

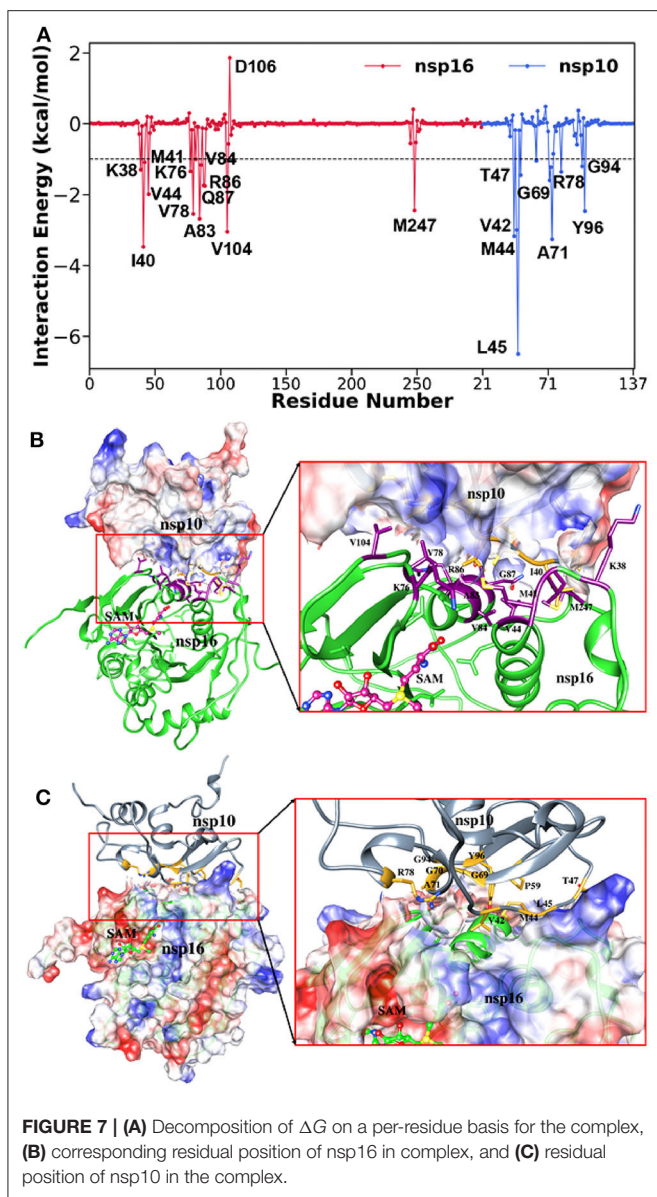
System	$\Delta E_{vdw}$	$\Delta E_{elec}$	$\Delta G_{pol}$	$\Delta G_{np}$	$\Delta G_{bind}$	$\Delta G_{bind}^a$
WT	-90.4 (0.2)	-429.4 (3.0)	481.7 (3.2)	-9.6 (0.0)	-47.7 (0.4)	
I40A	-86.0 (0.2)	-429.2 (3.0)	480.5 (3.2)	-9.5 (0.0)	-44.2 (0.4)	3.5 (1.2)
V44A	-88.0 (0.2)	-429.2 (3.0)	481.4 (3.2)	-9.6 (0.0)	-45.5 (0.4)	2.1 (1.5)
V78A	-87.5 (0.2)	-429.5 (3.0)	481.0 (3.2)	-9.5 (0.0)	-45.5 (0.4)	2.2 (1.5)
R86A	-87.5 (0.2)	-522.6 (3.0)	574.5 (3.3)	-9.5 (0.0)	-45.1 (0.4)	2.6 (2.5)
Q87A	-86.8 (0.2)	-416.9 (3.0)	466.8 (3.2)	-9.4 (0.0)	-46.2 (0.4)	1.5 (1.6)
V104A	-86.9 (0.2)	-429.7 (3.0)	481.11 (3.2)	-9.4 (0.0)	-44.9 (0.4)	2.8 (1.5)
M247A	-87.1 (0.2)	-428.5 (3.0)	479.0 (3.2)	-9.6 (0.0)	46.1 (0.4)	1.5 (0.8)

Along with the Computational Alanine-Scanning (CAS) mutagenesis results of the complex nsp16/nsp10. The binding energy is given in kcal/mol, and the standard error of the mean is provided in parentheses.

$$\Delta \Delta G_{bind}^a = \Delta G_{bind}^{mut} - \Delta G_{bind}^{WT}$$

in protein-protein or protein-ligand interactions (Jonniya et al., 2020; Roy et al., 2020; Sk et al., 2020d). Different H-bonds and hydrophobic interactions from the stable structure of the





nsp16-nsp10 obtained from the MD simulations were plotted via Ligplot (Wallace et al., 1995) and shown in **Figure 8**.

The percentage occupancy of the residual contacts with the cut-off 3.9 Å for the protein-protein is also listed in **Supplementary Table 4**. Overall, these results highlighted the significant residues forming strong interactions between nsp16 and nsp10, which may aid in the development and design of inhibitors that could block these protein-protein interactions by inhibiting the 2'-O-MTase activity.

## Computational Alanine Scanning

The changes in the binding free energy were computed as in Equation (4) (see Method section) after replacing the residue of WT to alanine. The impact of a single mutation in the protein-protein interaction is mainly reflected by the more positive value

**TABLE 6 |** The hydrogen bonds formed between nsp16 and nsp10 in the complex and the corresponding average distance and percent determined using the production trajectories in the MD simulations.

Binding couples		Molecular dynamics	
Acceptor	Donor...H	Distance (Å)	Occupancy (%)
Ala83@O	<b>Tyr96@OH...HH</b>	2.73	90.80
<b>Leu45@O</b>	Gln87@NE2...HE21	2.85	67.83
Asp106@OD1	<b>Ala71@N...H</b>	2.87	29.23
Asp106@OD1	<b>Gly94@N...H</b>	2.84	24.23
Lys38@O	<b>Lys43@NZ...HZ2</b>	2.80	25.28
Lys38@O	<b>Lys43@NZ...HZ3</b>	2.80	25.01
Lys38@O	<b>Lys43@NZ...HZ1</b>	2.80	23.63
Asp106@OD2	<b>Gly94@N...H</b>	2.84	17.58
Ser105@O	<b>Lys93@NZ...HZ3</b>	2.79	12.65
Ser105@O	<b>Lys93@NZ...HZ2</b>	2.79	12.35
Ser105@O	<b>Lys93@NZ...HZ1</b>	2.79	12.25

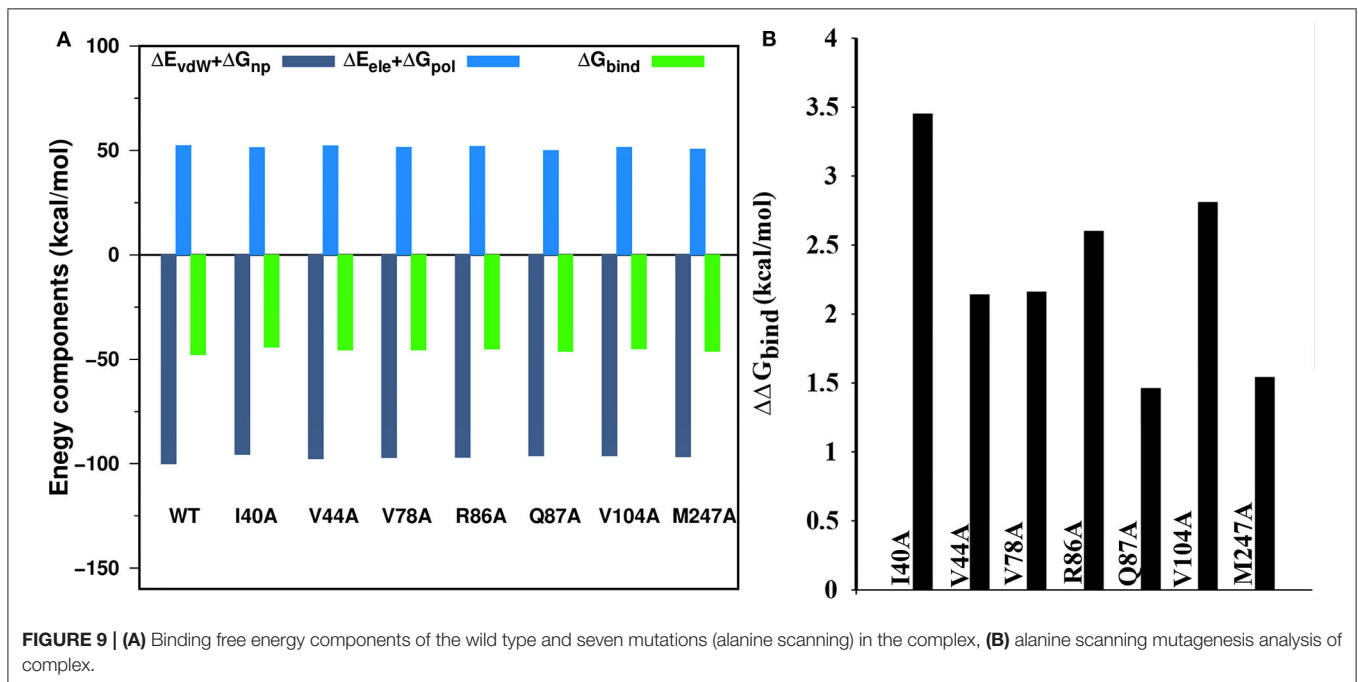
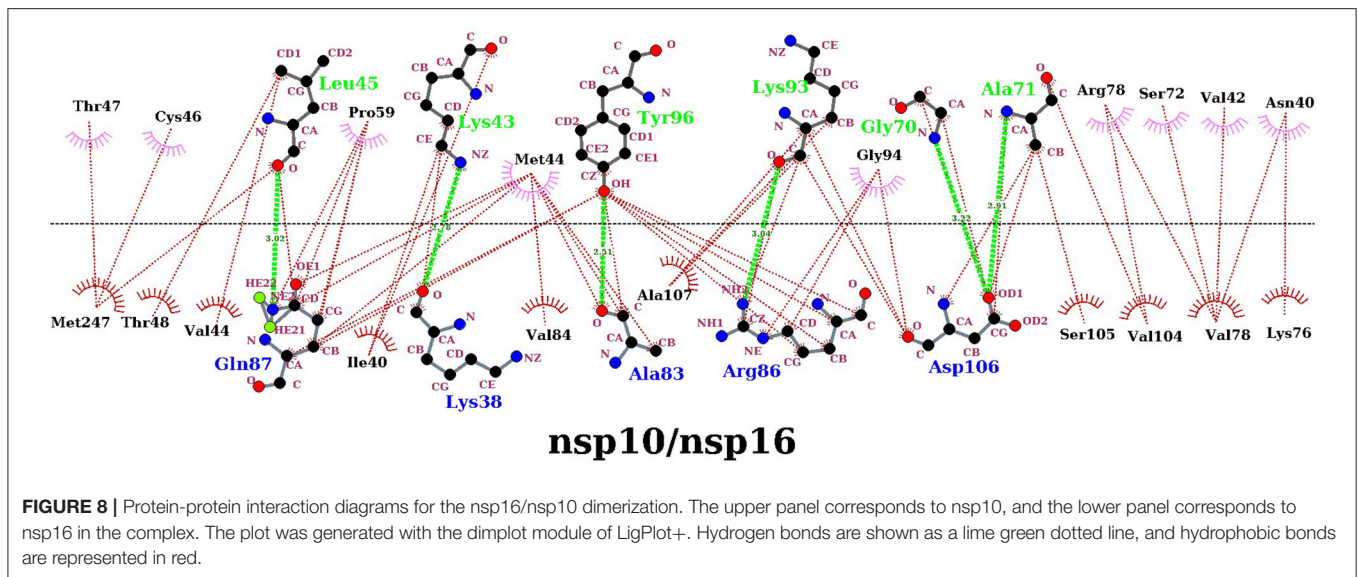
\* Bold letters belong to the nsp10 structure. Only H-bonds with more than 10% occupancy are listed.

of the  $\Delta\Delta G_{bind}$ . In our study, we have conducted CAS for nsp16 by considering those residues with the decomposition free energy  $> 1.5$  kcal/mol, as given in **Supplementary Table 3**. The binding free energy components calculated from the CAS mutagenesis for residues I40A, V104A, R86A, V78A, V44A, M247A, and Q87A of nsp16 are listed in **Table 5** and compared with the WT. As seen in **Supplementary Table 3**, although the  $\Delta G_{bind}$  of WT is higher than mutants, different energy components of mutants follow the same trend as WT. The  $\Delta E_{ele}$  is higher than  $\Delta E_{vdW}$ , but disfavoring polar solvation energy  $\Delta G_{pol}$  compensates  $\Delta E_{ele}$ . As shown in **Figure 9A**, for all the systems, the binding free energy is mainly coming from the hydrophobic interactions, where the total non-polar energy ( $\Delta E_{vdW} + \Delta G_{np}$ ) is higher than the total polar energy ( $\Delta E_{ele} + \Delta G_{pol}$ ). **Figure 9B** reflects significant residues in the protein interface calculated from CAS mutagenesis. It shows that  $\Delta\Delta G_{bind}$  for mutants, I40A, V104A, and R86A are comparatively high, suggesting that primarily these residues play a significant role in the heterodimer formation, which is in accordance with the decomposition of energy. The CAS mutagenesis results depict that in addition to hydrophobic residues I40 and V104, the hydrophilic residue R86 also plays a vital role in the binding of nsp10-nsp16.

## Temperature and Salt Concentration Effect on the Binding Affinity

Next, we investigated the effect of temperature and salt concentration in the binding of nsp16/nsp10 and nsp16/nsp10/SAM using the MM-PBSA method. This method presents itself to be a perfect model to study the effect of conformational dynamics of the same protein evolved in different environmental conditions to the fate of the ligand, ultimately decided by the binding affinity or dissociation.

**Supplementary Tables 5, 6** displayed the binding free energy components for nsp16-nsp10 and nsp16/nsp10/SAM, respectively, at two different temperatures. As shown in



**Supplementary Table 5**, the predicted binding free energies between nsp10 and nsp16 ( $\Delta G_{bind}$ ) was found to be  $-47.7$  kcal/mol, and  $-52.2$  kcal/mol at 300 and 310 K, respectively. It suggests that nsp16 binds more strongly to nsp10 at 310 K than 300 K. It can also be noted from **Supplementary Table 5** that at the elevated temperature (310 K), the magnitude of total polar interactions ( $\Delta E_{ele} + \Delta G_{pol}$ ) decreases (52.3 to 49.6 kcal/mol) and oppose less unfavorably to the protein-protein association. At a higher temperature, the non-polar interactions ( $\Delta E_{vdW} + \Delta G_{np}$ ) decreased from  $-100$  to  $-102$  kcal/mol and contributed more favorably to the association of nsp16-nsp10. Similarly, **Supplementary Table 6** suggested

that the estimated binding free energies (without entropy) of the cofactor SAM with nsp16/nsp10 ( $\Delta G_{bind}$ ) were  $-46.6$  and  $-13.2$  kcal/mol at 300 and 310 K, respectively. It was further evident from **Supplementary Table 6** that after increasing the temperature, the binding affinity of SAM toward nsp16/nsp10 decreased. At room temperature (300 K) both total polar ( $\Delta E_{ele} + \Delta G_{pol} = -2.1$  kcal/mol) and non-polar ( $\Delta E_{vdW} + \Delta G_{np} = -44.5$  kcal/mol) interactions favored the binding of SAM with nsp16. After increasing the temperature to 310 K, the total polar interaction ( $\Delta E_{ele} + \Delta G_{pol}$ ) became unfavorable to the binding of SAM to nsp16/nsp10. However, the total non-polar contribution ( $\Delta E_{vdW} + \Delta G_{np}$ ) still favored the binding. As

compared to room temperature, the strength of the non-polar ( $\Delta E_{vdW} + \Delta G_{np}$ ) interactions decreases significantly ( $-44.5$  to  $-23.5$  kcal/mol). At 310 K, we have noticed that up to 400 ns, SAM binds strongly to nsp16. After that, SAM got detached from the binding cavity (see **Supplementary Figure 8**).

The salt concentration also influenced the protein-protein interactions as well as the binding of SAM to nsp16/nsp10, which are evident from **Supplementary Tables 5, 6**. As shown in **Supplementary Table 5**, the predicted binding free energies of nsp10 with nsp16 ( $\Delta G_{bind}$ ) were found to be  $-44.8$  and  $-37.7$  kcal/mol, for the salt concentration of 0.15 and 0.25 M, respectively. After increasing the salt concentration, it was observed that the total polar ( $\Delta E_{ele} + \Delta G_{pol}$ ) and non-polar interactions ( $\Delta E_{vdW} + \Delta G_{np}$ ) increased from 54.1 to 55.3 kcal/mol and  $-98.9$  to  $-93$  kcal/mol, respectively. The rise in unfavorable interactions caused the destabilization of the protein-protein interactions. Similarly, the binding of SAM to the heterodimer was found to be affected by the increased salt concentration (see **Supplementary Table 6**). The estimated binding free energy of SAM ( $\Delta G_{bind}$ ) was  $-23.7$  and  $-22.1$  kcal/mol for the salt concentration of 0.15 and 0.25 M, respectively. These values are significantly higher than what was obtained for the neutral salt concentration ( $-46.6$  kcal/mol).  $\Delta E_{vdW}$  and  $\Delta E_{elec}$  were found to contribute less favorably to the binding of SAM to nsp16/nsp10 in comparison to neutral simulations. A similar trend was observed when the temperature was increased from 300 to 310 K. The time evolution of CoM distance between nsp16 and SAM was displayed in **Supplementary Figure 9**. It is evident from **Supplementary Figure 9** that with the increased salt concentration, the CoM distance between nsp16 and SAM increased and remained stable around 17 Å and 18 Å for 0.15 and 0.25 M, respectively. This implies that the cofactor SAM moves away from the binding cavity with the increased salt concentration.

## CONCLUSIONS

Herein, we have employed extensive MD simulations of 1  $\mu$ s along with the molecular mechanics/Poisson-Boltzmann surface area (MM/PBSA) method to study the binding mechanism of the cofactor SAM to the nsp16/nsp10 heterodimer and sub-unit nsp16 alone (nsp16<sub>SAM</sub>) of SARS-CoV-2. Our MD/MMPBSA calculations suggested that SAM binds strongly to the nsp16/nsp10 heterodimer and fails to bind to the nsp16 monomer. It emphasized that nsp10 helps in the strong interaction between SAM and nsp16 to execute the 2'-O-MTase activity. This finding agrees well with the experimental study, and a similar observation was made for other coronaviruses, including SARS-CoV and MERS-CoV. We have also investigated the interactions between nsp16 and nsp10. Our study revealed that the binding of nsp10 stabilizes the complex (nsp16/nsp10) structure. Further, our study showed that hydrophobic interactions are critical for the heterodimer association. Thus, apart from the active site of nsp16, the

interface of nsp16/nsp10 can also be considered as a potential target site in the design of antiviral drugs such as peptide inhibitors. It includes Ile40, Val104, Ala83, Val78, Met247, Val44, Gln87, Arg86, Lys76, Lys38, Val84, and Met41 from nsp16, and Leu45, Ala71, Val42, Met44, Tyr96, Gly69, Thr47, Arg78, Gly70, Gly94, and Pro59 from nsp10. Besides, the stable hydrogen bond between Ala83 (nsp16) and Tyr96 (nsp10), and between Gln87 (nsp16) and Leu45 (nsp10) were important in the nsp16-nsp10 interface. The CAS study reveals that residues I40A, V104A, R86A, V78A, V44A, M247A, and Q87A of nsp16 were considered as hot spot residues for the association of nsp16-nsp10.  $\Delta\Delta G_{bind}$  for mutants, I40A, V104A, and R86A are comparatively high, suggesting the significance of these residues. Finally, we investigated the effect of temperature and salt concentration on the binding of SAM to the heterodimer. Our study revealed that the SAM binding was impaired due to an increase in temperature or salt concentration. Finally, our study provides a comprehensive understanding of the dynamic and thermodynamic process of binding nsp16 and nsp10 that will contribute to the rational design of inhibitors targeting nsp16/nsp10.

## DATA AVAILABILITY STATEMENT

The raw data supporting the conclusions of this article will be made available by the authors, without undue reservation.

## AUTHOR CONTRIBUTIONS

Project conceived and supervised by PK. Simulations and analyses were performed by MS, NJ, RR, and SP. Manuscript was written by MS, NJ, and PK. All authors contributed to the article and approved the submitted version.

## FUNDING

This work was partially supported by the Department of Biotechnology, Govt. of India (Grant number BT/RLF/RE-entry/40/2014, DBT Ramalingaswami Re-entry Fellowship), and Department of Science and Technology (DST), Govt. of India (Grant number ECR/2017/000010). MS would like to thank DST, Govt. of India, for providing fellowship under the INSPIRE Fellowship Scheme (DST/INSPIRE Fellowship/2017/IF170145).

## ACKNOWLEDGMENTS

This manuscript has been released as a pre-print at ChemRxiv (Sk et al., 2020b).

## SUPPLEMENTARY MATERIAL

The Supplementary Material for this article can be found online at: <https://www.frontiersin.org/articles/10.3389/fmolb.2020.590165/full#supplementary-material>



## REFERENCES

- Amadei, A., Linssen, A., de Groot, B., van Aalten, D., and Berendsen, H. (1996). An efficient method for sampling the essential subspace of proteins. *J. Biomol. Struct. Dyn.* 13, 615–625. doi: 10.1080/07391102.1996.10508874
- Arabi, Y., Harthi, A., Hussein, J., Bouchama, A., Johani, S., Hajeer, A., et al. (2015). Severe neurologic syndrome associated with Middle East respiratory syndrome corona virus (MERS-CoV). *Infection* 43, 495–501. doi: 10.1007/s15010-015-0720-y
- Berendsen, H. J., Postma, J. V., van Gunsteren, W. F., Dinola, A., and Haak, J. (1984). Molecular dynamics with coupling to an external bath. *J. Chem. Phys.* 81, 3684–3690. doi: 10.1063/1.448118
- Bogoch, I. I., Watts, A., Thomas-Bachli, A., Huber, C., Kraemer, M. U., and Khan, K. (2020). Potential for global spread of a novel coronavirus from China. *J Travel Med.* 27:taaa011. doi: 10.1093/jtm/taaa011
- Carlsson, J., and Åqvist, J. (2006). Calculations of solute and solvent entropies from molecular dynamics simulations. *Phys Chem. Chem. Phys.* 8, 5385–5395. doi: 10.1039/B608486A
- Case, D. A., Huang, Y., Ben-Shalom, S. R., Brozell, D. S., Cerutti, T. E., Cheatham, I., et al. (2018). *AMBER 2018*. San Francisco, CA: University of California.
- Chakrabarty, B., Naganathan, V., Garg, K., Agarwal, Y., and Parekh, N. (2019). NAPS update: network analysis of molecular dynamics data and protein–nucleic acid complexes. *Nucleic Acids Res.* 47, W462–W470. doi: 10.1093/nar/gkz399
- Chen, Y., Su, C., Ke, M., Jin, X., Xu, L., Zhang, Z., et al. (2011). Biochemical and structural insights into the mechanisms of SARS coronavirus RNA ribose 2'-O-methylation by nsp16/nsp10 protein complex. *PLoS Pathog.* 7:e1002294. doi: 10.1371/journal.ppat.1002294
- Chen, Y. W., Yiu, C.-P. B., and Wong, K.-Y. (2020). Prediction of the SARS-CoV-2 (2019-nCoV) 3C-like protease (3CL pro) structure: virtual screening reveals velpatasvir, ledipasvir, and other drug repurposing candidates. *Frontiers in Molecular Biosciences* 9:129. doi: 10.12688/f1000research.22457.2
- Coleman, C. M., and Frieman, M. B. (2014). Coronaviruses: important emerging human pathogens. *J. Virol.* 88, 5209–5212. doi: 10.1128/JVI.03488-13
- Darden, T., York, D., and Pedersen, L. (1993). Particle mesh Ewald: An N · log(N) method for Ewald sums in large systems. *J. Chem. Phys.* 98, 10089–10092. doi: 10.1063/1.464397
- Eckerle, L. D., Becker, M. M., Halpin, R. A., Li, K., Venter, E., Lu, X., et al. (2010). Infidelity of SARS-CoV Nsp14-exonuclease mutant virus replication is revealed by complete genome sequencing. *PLoS Pathog.* 6:e1000896. doi: 10.1371/journal.ppat.1000896
- Egloff, M. P., Benarroch, D., Selisko, B., Romette, J. L., and Canard, B. (2002). An RNA cap (nucleoside-2'-O)-methyltransferase in the flavivirus RNA polymerase NS5: crystal structure and functional characterization. *EMBO J.* 21, 2757–2768. doi: 10.1093/emboj/21.11.2757
- Fehr, A. R., and Perlman, S. (2015). “Coronaviruses: an overview of their replication and pathogenesis,” in *Coronaviruses. Methods in Molecular Biology*, Vol. 1282, eds H. Maier, E. Bickerton, and P. Britton (New York, NY: Humana Press), 1–23. doi: 10.1007/978-1-4939-2438-7\_1
- Frauenfelder, H., Sligar, S. G., and Wolynes, P. G. (1991). The energy landscapes and motions of proteins. *Science* 254, 1598–1603. doi: 10.1126/science.1749933
- Furuichi, Y., and Shatkin, A. J. (2000). Viral and cellular mRNA capping: past and prospects. *Adv. Virus Res.* 55:135. doi: 10.1016/S0065-3527(00)55003-9
- Gohlke, H., Kiel, C., and Case, D. A. (2003). Insights into protein–protein binding by binding free energy calculation and free energy decomposition for the Ras–Raf and Ras–RalGDS complexes. *J. Mol. Biol.* 330, 891–913. doi: 10.1016/S0022-2836(03)00610-7
- Guan, W. J., Ni, Z. Y., Hu, Y., Liang, W. H., Ou, C. Q., He, J. X., et al. (2020). Clinical Characteristics of Coronavirus Disease 2019 in China. *N Engl J Med.* 382, 1708–1720. doi: 10.1056/NEJMoa2002032
- Harcourt, B. H., Jukneliene, D., Kanjanahaluethai, A., Bechill, J., Severson, K. M., Smith, C. M., et al. (2004). Identification of severe acute respiratory syndrome coronavirus replicase products and characterization of papain-like protease activity. *J. Virol.* 78, 13600–13612. doi: 10.1128/JVI.78.24.13600-13612.2004
- Hawkins, G. D., Cramer, C. J., and Truhlar, D. G. (1995). Pairwise solute descreening of solute charges from a dielectric medium. *Chem. Phys. Lett.* 246, 122–129. doi: 10.1016/0009-2614(95)01082-K
- Hawkins, G. D., Cramer, C. J., and Truhlar, D. G. (1996). Parametrized models of aqueous free energies of solvation based on pairwise descreening of solute atomic charges from a dielectric medium. *J. Phys. Chem.* 100, 19824–19839. doi: 10.1021/jp961710n
- Hou, T., Wang, J., Li, Y., and Wang, W. (2011). Assessing the performance of the MM/PBSA and MM/GBSA methods. 1. The accuracy of binding free energy calculations based on molecular dynamics simulations. *J. Chem. Inf. Model.* 51, 69–82. doi: 10.1021/ci100275a
- Hu, G., Ma, A., Dou, X., Zhao, L., and Wang, J. J. (2016). Computational studies of a mechanism for binding and drug resistance in the wild type and four mutations of HIV-1 protease with a GRL-0519 inhibitor. *Int. J. Mol. Sci.* 17:819. doi: 10.3390/ijms17060819
- Huang, C., Wang, Y., Li, X., Ren, L., Zhao, J., Hu, Y., et al. (2020). Clinical features of patients infected with 2019 novel coronavirus in Wuhan, China. *Lancet* 395, 497–506. doi: 10.1016/S0140-6736(20)30183-5
- Ichiye, T., and Karplus, M. (1991). Collective motions in proteins: a covariance analysis of atomic fluctuations in molecular dynamics and normal mode simulations. *Proteins* 11, 205–217. doi: 10.1002/prot.340110305
- Jakalian, A., Jack, D. B., and Bayly, C. I. (2002). Fast, efficient generation of high-quality atomic charges. AM1-BCC model: II. Parameterization and validation. *J. Comput. Chem.* 23, 1623–1641. doi: 10.1002/jcc.10128
- Jeffrey, G. A. (1997). *An Introduction to Hydrogen Bonding*. New York, NY: Oxford University Press.
- Jonniya, N. A., and Kar, P. (2020). Investigating specificity of the anti-hypertensive inhibitor WNK463 against With-No-Lysine kinase family isoforms via multiscale simulations. *J. Biomol. Struct. Dyn.* 38, 1306–1321. doi: 10.1080/07391102.2019.1602079
- Jonniya, N. A., Sk, M. F., and Kar, P. (2019). Investigating phosphorylation-induced conformational changes in WNK1 kinase by molecular dynamics simulations. *ACS Omega* 4, 17404–17416. doi: 10.1021/acsomega.9b02187
- Jonniya, N. A., Sk, M. F., and Kar, P. (2020). A comparative study of structural and conformational properties of WNK kinase isoforms bound to an inhibitor: insights from molecular dynamic simulations. *J. Biomol. Struct. Dyn.* doi: 10.1080/07391102.2020.1827035. [Epub ahead of print].
- Kar, P., and Knecht, V. (2012a). Energetic basis for drug resistance of HIV-1 protease mutants against amprevir. *J. Comput. Aided Mol. Des.* 26, 215–232. doi: 10.1007/s10822-012-9550-5
- Kar, P., and Knecht, V. (2012b). Energetics of mutation-induced changes in potency of lersivirine against HIV-1 reverse transcriptase. *J. Phys. Chem. B* 116, 6269–6278. doi: 10.1021/jp300818c
- Kar, P., and Knecht, V. (2012c). Origin of decrease in potency of darunavir and two related antiviral inhibitors against HIV-2 compared to HIV-1 protease. *J. Phys. Chem. B* 116, 2605–2614. doi: 10.1021/jp211768n
- Kar, P., and Knecht, V. (2012d). Mutation-induced loop opening and energetics for binding of tamiflu to influenza N8 neuraminidase. *J. Phys. Chem. B* 116, 6137–6149. doi: 10.1021/jp3022612
- Kar, P., Lipowsky, R., and Knecht, V. (2011). Importance of polar solvation for cross-reactivity of antibody and its variants with steroids. *J. Phys. Chem. B* 115, 7661–7669. doi: 10.1021/jp201538t
- Kar, P., Lipowsky, R., and Knecht, V. (2013). Importance of polar solvation and configurational entropy for design of antiretroviral drugs targeting HIV-1 protease. *J. Phys. Chem. B* 117, 5793–5805. doi: 10.1021/jp3085292
- Kar, P., Seel, M., Hansmann, U. H., and Höfinger, S. (2007a). Dispersion terms and analysis of size- and charge dependence in an enhanced poisson– Boltzmann approach. *J. Phys. Chem. B* 111, 8910–8918. doi: 10.1021/jp072302u
- Kar, P., Wei, Y., Hansmann, U. H., and Höfinger, S. (2007b). Systematic study of the boundary composition in Poisson Boltzmann calculations. *J. Comput. Chem.* 28, 2538–2544. doi: 10.1002/jcc.20698
- Karplus, M., and Kushick, J. N. (1981). Method for estimating the configurational entropy of macromolecules. *Macromolecules* 14, 325–332. doi: 10.1021/ma50003a019
- King, A. M. Q., Adams, M. J., Carstens, E. B., and Lefkowitz, E. J. (2011). *Virus Taxonomy: 9th Report of the International Committee on Taxonomy of Viruses*. San Diego, CA: Academic Press
- Kollman, P. A., Massova, I., Reyes, C., Kuhn, B., Huo, S., Chong, L., et al. (2000). Calculating structures and free energies of complex molecules: combining

- molecular mechanics and continuum models. *Acc. Chem. Res.* 33, 889–897. doi: 10.1021/ar000033j
- Kozakov, D., Grove, L. E., Hall, D. R., Bohnuud, T., Mottarella, S. E., Luo, L., et al. (2015). The FTMap family of web servers for determining and characterizing ligand-binding hot spots of proteins. *Nat. Protoc.* 10, 733–755. doi: 10.1038/nprot.2015.043
- Kräutler, V., van Gunsteren, W. F., and Hünenberger, P. H. (2001). A fast SHAKE algorithm to solve distance constraint equations for small molecules in molecular dynamics simulations. *J. Comput. Chem.* 22, 501–508. doi: 10.1002/1096-987X(20010415)22:5<501::AID-JCC1021>3.0.CO;2-V
- Kyte, J., and Doolittle, R. F. (1982). A simple method for displaying the hydrophobic character of a protein. *J. Mol. Biol.* 157, 105–132. doi: 10.1016/0022-2836(82)90515-0
- Lin, S., Chen, H., Ye, F., Chen, Z., Yang, F., Zheng, Y., et al. (2020). Crystal structure of SARS-CoV-2 nsp10/nsp16 2'-O-methylase and its implication on antiviral drug design. *Signal Transduct Target Ther.* 5:131. doi: 10.1038/s41392-020-00241-4
- Lin, X., Gong, Z., Xiao, Z., Xiong, J., Fan, B., and Liu, J. (2020). Novel coronavirus pneumonia outbreak in 2019: computed tomographic findings in two cases. *Korean J. Radiol.* 21, 365–368. doi: 10.3348/kjr.2020.0078
- Loncharich, R. J., Brooks, B. R., and Pastor, R. W. (1992). Langevin dynamics of peptides: the frictional dependence of isomerization rates of N-acetylalanine-N'-methylamide. *Biopolymers* 32, 523–535. doi: 10.1002/bip.360320508
- Lu, H. (2020). Drug treatment options for the 2019-new coronavirus (2019-nCoV). *Biosci. Trends* 14, 69–71. doi: 10.5582/bst.2020.01020
- Lu, R., Zhao, X., Li, J., Niu, P., Yang, B., Wu, H., et al. (2020). Genomic characterisation and epidemiology of 2019 novel coronavirus: implications for virus origins and receptor binding. *Lancet* 395, 565–574. doi: 10.1016/S0140-6736(20)30251-8
- Lun, Z.-R., and Qu, L.-H. (2004). Animal-to-human SARS-associated coronavirus transmission? *Emerg Infect Dis.* 10:959. doi: 10.3201/eid1005.040022
- Machado, M. R., and Pantano, S. (2020). Split the charge difference in two! a rule of thumb for adding proper amounts of ions in MD simulations. *J. Chem. Theory Comput.* 16, 1367–1372. doi: 10.1021/acs.jctc.9b00953
- Maier, J. A., Martinez, C., Kasavajhala, K., Wickstrom, L., Hauser, K. E., and Simmerling, C. (2015). ff14SB: improving the accuracy of protein side chain and backbone parameters from ff99SB. *J. Chem. Theory Comput.* 11, 3696–3713. doi: 10.1021/acs.jctc.5b00255
- Massova, I., and Kollman, P. A. (1999). Computational alanine scanning to probe protein-protein interactions: a novel approach to evaluate binding free energies. *J. Am. Chem. Soc.* 121, 8133–8143. doi: 10.1021/ja990935j
- Minasov, G., Shuvalova, L., Rosas-Lemus, M., Kiryukhina, O., Wiersum, G., Godzik, A., et al. (2020). 1.80 Angstrom Resolution Crystal Structure of NSP16 - NSP10 Complex from SARS-CoV-2. Available online at: <http://www.rcsb.org/structure/6W4H> (accessed March 18, 2020).
- Moreira, I. S., Fernandes, P. A., and Ramos, M. J. (2007). Computational alanine scanning mutagenesis—an improved methodological approach. *J. Comput. Chem.* 28, 644–654. doi: 10.1002/jcc.20566
- Olsson, M. H., Søndergaard, C. R., Rostkowski, M., and Jensen, J. H. (2011). PROPKA3: consistent treatment of internal and surface residues in empirical pK<sub>a</sub> predictions. *J. Chem. Theory Comput.* 7, 525–537. doi: 10.1021/ct100578z
- Pastor, R. W., Brooks, B. R., and Szabo, A. (1988). An analysis of the accuracy of Langevin and molecular dynamics algorithms. *Mol. Phys.* 65, 1409–1419. doi: 10.1080/00268978800101881
- Pillaiyar, T., Meenakshisundaram, S., and Manickam, M. (2020). Recent Discovery and Development of Inhibitors Targeting Coronaviruses. *Drug Discov. Today.* 25, 668–688. doi: 10.1016/j.drudis.2020.01.015
- Price, D. J., and Brooks, C. L. III. (2004). A modified TIP3P water potential for simulation with Ewald summation. *J. Chem. Phys.* 121, 10096–10103. doi: 10.1063/1.1808117
- Rempe, S. B., and Jónsson, H. (1998). A computational exercise illustrating molecular vibrations and normal modes. *Chem. Educ.* 3, 1–17. doi: 10.1007/s00897980231a
- Roe, D. R., and Cheatham, T. E. III. (2013). PTRAJ and CPPTRAJ: software for processing and analysis of molecular dynamics trajectory data. *J. Chem. Theory Comput.* 9, 3084–3095. doi: 10.1021/ct400341p
- Rosas-Lemus, M., Minasov, G., Shuvalova, L., Inniss, N.L., Kiryukhina, O., Wiersum, G., et al. (2020). The crystal structure of nsp10-nsp16 heterodimer from SARS-CoV-2 in complex with S-adenosylmethionine. *bioRxiv*. doi: 10.1101/2020.04.17.047498
- Roy, R., Ghosh, B., and Kar, P. (2020). Investigating conformational dynamics of lewis Y oligosaccharides and elucidating blood group dependency of cholera using molecular dynamics. *ACS Omega* 5, 3932–3942. doi: 10.1021/acsomega.9b03398
- Sanachai, K., Mahalapbutr, P., Choowongkamon, K., Poo-Arporn, R. P., Wolschann, P., and Rungrotmongkol, T. (2020). Insights into the binding recognition and susceptibility of tofacitinib toward janus kinases. *ACS Omega* 5, 369–377. doi: 10.1021/acsomega.9b02800
- Sheahan, T., Sims, A., Leist, S., Schäfer, A., Won, J., Brown, A., et al. (2020). Comparative therapeutic efficacy of remdesivir and combination lopinavir, ritonavir, and interferon beta against MERS-CoV. *Nat. Commun.* 11:222. doi: 10.1038/s41467-019-13940-6
- Shi, S., Zhang, S., and Zhang, Q. (2018). Insight into binding mechanisms of inhibitors MKP56, MKP73, MKP86, and MKP97 to HIV-1 protease by using molecular dynamics simulation. *J. Biomol. Struct. Dyn.* 36, 981–992. doi: 10.1080/07391102.2017.1305296
- Singh, S., Sk, M. F., Sonawane, A., Kar, P., and Sadhukhan, S. (2020). Plant-derived natural polyphenols as potential antiviral drugs against SARS-CoV-2 via RNA-dependent RNA polymerase (RdRp) inhibition: an *in-silico* analysis. *J. Biomol. Struct. Dyn.* doi: 10.1080/07391102.2020.1796810. [Epub ahead of print].
- Sk, M. F., Jonniya, N. A., and Kar, P. (2020a). Exploring the energetic basis of binding of currently used drugs against HIV-1 subtype CRF01\_AE protease via molecular dynamics simulations. *J. Biomol. Struct. Dyn.* doi: 10.1080/07391102.2020.1794965. [Epub ahead of print].
- Sk, M. F., Jonniya, N. A., Roy, R., Poddar, S., and Kar, P. (2020b). Computational investigation of structural dynamics of SARS-CoV-2 methyltransferase-stimulatory factor heterodimer nsp16/nsp10 bound to the cofactor SAM. *ChemRxiv [Preprint]*. doi: 10.26434/chemrxiv.12608795.v1
- Sk, M. F., Roy, R., Jonniya, N. A., Poddar, S., and Kar, P. (2020c). Elucidating biophysical basis of binding of inhibitors to SARS-CoV-2 main protease by using molecular dynamics simulations and free energy calculations. *J. Biomol. Struct. Dyn.* doi: 10.26434/chemrxiv.12084207. [Epub ahead of print].
- Sk, M. F., Roy, R., and Kar, P. (2020d). Exploring the potency of currently used drugs against HIV-1 protease of subtype D variant by using multiscale simulations. *J. Biomol. Struct. Dyn.* doi: 10.1080/07391102.2020.1724196. [Epub ahead of print].
- Viswanathan, T., Arya, S., Chan, S. H., Qi, S., Dai, N., Misra, A., et al. (2020). Structural basis of RNA cap modification by SARS-CoV-2. *Nat. Commun.* 11:3718. doi: 10.1038/s41467-020-17496-8
- Wallace, A. C., Laskowski, R. A., and Thornton, J. M. (1995). LIGPLOT: a program to generate schematic diagrams of protein-ligand interactions. *Protein Eng. Design Select.* 8, 127–134. doi: 10.1093/protein/8.2.127
- Wang, J., Wang, W., Kollman, P. A., and Case, D. A. (2006). Automatic atom type and bond type perception in molecular mechanical calculations. *J. Mol. Graphics Model.* 25, 247–260. doi: 10.1016/j.jmglm.2005.12.005
- Wang, J., Wolf, R. M., Caldwell, J. W., Kollman, P. A., and Case, D. A. (2004). Development and testing of a general amber force field. *J. Comput. Chem.* 25, 1157–1174. doi: 10.1002/jcc.20035
- Wang, Y., Sun, Y., Wu, A., Xu, S., Pan, R., Zeng, C., et al. (2015). Coronavirus nsp10/nsp16 methyltransferase can be targeted by nsp10-derived peptide *in vitro* and *in vivo* to reduce replication and pathogenesis. *J. Virol.* 89, 8416–8427. doi: 10.1128/JVI.00948-15
- Weiser, J., Shenkin, P. S., and Still, W. C. (1999). Fast, approximate algorithm for detection of solvent-inaccessible atoms. *J. Comput. Chem.* 20, 586–596.
- Weiss, S. R., and Leibowitz, J. L. (2011). “Coronavirus pathogenesis,” in *Advances in Virus Research*, eds K. Maramorosch, A. J. Shatkin, and F. A. Murphy (Elsevier) 81, 85–164. doi: 10.1016/B978-0-12-385885-6.00009-2
- Weiss, S. R., and Navas-Martin, S. (2005). Coronavirus pathogenesis and the emerging pathogen severe acute respiratory syndrome coronavirus. *Microbiol. Mol. Biol. Rev.* 69, 635–664. doi: 10.1128/MMBR.69.4.635-664.2005
- Woo, P. C., Huang, Y., Lau, S. K., and Yuen, K.-Y. (2010). Coronavirus genomics and bioinformatics analysis. *Viruses* 2, 1804–1820. doi: 10.3390/v2010081803

- Wu, C., Liu, Y., Yang, Y., Zhang, P., Zhong, W., Wang, Y., et al. (2020). Analysis of therapeutic targets for SARS-CoV-2 and discovery of potential drugs by computational methods. *Acta Pharm. Sinica B* 10, 766–788. doi: 10.1016/j.apsb.2020.02.008
- Xu, B., Shen, H., Zhu, X., and Li, G. (2011). Fast and accurate computation schemes for evaluating vibrational entropy of proteins. *J. Comput. Chem.* 32, 3188–3193. doi: 10.1002/jcc.21900
- Yang, H., Xie, W., Xue, X., Yang, K., Ma, J., Liang, W., et al. (2005). Design of wide-spectrum inhibitors targeting coronavirus main proteases. *PLoS Biol* 3:e324. doi: 10.1371/journal.pbio.0030428
- Zeng, Z. Q., Chen, D. H., Tan, W. P., Qiu, S. Y., Xu, D., Liang, H. X., et al. (2018). Epidemiology and clinical characteristics of human coronaviruses OC43, 229E, NL63, and HKU1: a study of hospitalized children with acute respiratory tract infection in Guangzhou, China. *Eur. J. Clin. Microbiol. Infect. Dis.* 37, 363–369. doi: 10.1007/s10096-017-3144-z
- Zhou, P., Yang, X. L., Wang, X. G., Hu, B., Zhang, L., Zhang, W., et al. (2020). A pneumonia outbreak associated with a new coronavirus of probable bat origin. *Nature* 579, 270–273. doi: 10.1038/s41586-020-2012-7
- Zhou, Y., Hou, Y., Shen, J., Huang, Y., Martin, W., and Cheng, F. (2020). Network-based drug repurposing for novel coronavirus 2019-nCoV/SARS-CoV-2. *Cell Discov.* 6:14. doi: 10.1038/s41421-020-0153-3

**Conflict of Interest:** The authors declare that the research was conducted in the absence of any commercial or financial relationships that could be construed as a potential conflict of interest.

Copyright © 2020 Sk, Jonniya, Roy, Poddar and Kar. This is an open-access article distributed under the terms of the Creative Commons Attribution License (CC BY). The use, distribution or reproduction in other forums is permitted, provided the original author(s) and the copyright owner(s) are credited and that the original publication in this journal is cited, in accordance with accepted academic practice. No use, distribution or reproduction is permitted which does not comply with these terms.